

The Community Land Model and Its Climate Statistics as a Component of the Community Climate System Model

ROBERT E. DICKINSON,* KEITH W. OLESON,+ GORDON BONAN,+ FORREST HOFFMAN,#
PETER THORNTON,+ MARIANA VERTENSTEIN,+ ZONG-LIANG YANG,@ AND XUBIN ZENG&

*Georgia Institute of Technology, Atlanta, Georgia

+National Center for Atmospheric Research, Boulder, Colorado

#Oak Ridge National Laboratory, Oak Ridge, Tennessee

@University of Texas at Austin, Austin, Texas

&The University of Arizona, Tucson, Arizona

(Manuscript received 23 January 2005, in final form 10 August 2005)

ABSTRACT

Several multidecadal simulations have been carried out with the new version of the Community Climate System Model (CCSM). This paper reports an analysis of the land component of these simulations. Global annual averages over land appear to be within the uncertainty of observational datasets, but the seasonal cycle over land of temperature and precipitation appears to be too weak. These departures from observations appear to be primarily a consequence of deficiencies in the simulation of the atmospheric model rather than of the land processes. High latitudes of northern winter are biased sufficiently warm to have a significant impact on the simulated value of global land temperature. The precipitation is approximately doubled from what it should be at some locations, and the snowpack and spring runoff are also excessive. The winter precipitation over Tibet is larger than observed. About two-thirds of this precipitation is sublimated during the winter, but what remains still produces a snowpack that is very large compared to that observed with correspondingly excessive spring runoff. A large cold anomaly over the Sahara Desert and Sahel also appears to be a consequence of a large anomaly in downward longwave radiation; low column water vapor appears to be most responsible. The modeled precipitation over the Amazon basin is low compared to that observed, the soil becomes too dry, and the temperature is too warm during the dry season.

1. Introduction

The inclusion of land in climate system models has much advanced in realism and complexity since its introduction by Manabe (1969) (e.g., Sellers et al. 1997). All such models are constrained by principles of mass and energy conservation and by observational data, and have used global maps of land cover (e.g., Matthews 1983; Wilson and Henderson-Sellers 1985) to correlate with observational data. Bonan et al. (2002) reviewed a previous manifestation of the particular model we report on here, the Community Land Model (CLM). The current version of the land model, CLM3, has significantly improved over its earlier versions as a result of

algorithmic improvements, better input from its parent atmosphere, and use of a higher spatial resolution by its parent model. The total system, the Community Climate System Model version 3 (CCSM3), is to be a major contributor to the Fourth Assessment Report (AR4) by the Intergovernmental Panel on Climate Change [IPCC; i.e., the follow-up to the Third Assessment Report (TAR) as reported by Houghton et al. (2001)]. Thus, it is important to scrutinize CLM3 scientifically as thoroughly as possible. Such an examination is the primary purpose of the present paper. What is good? What is still not as good as we would like? What scientific advances are likely to most benefit this model in the near future?

Development of a land model was first initiated at the National Center for Atmospheric Research (NCAR) more than two decades ago (e.g., Dickinson et al. 1986), but such a treatment has only become an accepted standard component of NCAR models with the introduc-

Corresponding author address: Dr. Robert E. Dickinson, School of Earth and Atmospheric Sciences, Georgia Institute of Technology, 221 Bobby Dodd Way, Atlanta, GA 30332.
E-mail: robted@eas.gatech.edu

TABLE 1. Description of simulations analyzed for this paper. The left column is the name given to a simulation (model and its resolutions). The other columns show what component models it uses.

| Simulation | Component models | | | | Years analyzed |
|---------------|------------------|--------|-----------------------|--------------------------|----------------|
| | Atmosphere | Land | Ice | Ocean | |
| CCSM3.0_T85 | CAM3.0 | CLM3.0 | CSIM5.0 ^a | CCSM3.0 POP ^b | 401–450 |
| CCSM3.0_T42 | CAM3.0 | CLM3.0 | CSIM5.0 | CCSM3.0 POP | 601–650 |
| CAM3/CLM3_T85 | CAM3.0 | CLM3.0 | CAM CSIM ^c | CAM docn ^d | 11–50 |
| CCSM2.0_T85 | CAM2.0 | CLM2.0 | CSIM4.0 | CCSM2.0 POP | 601–650 |
| CCM3/CLM2_T42 | CCM3 | CLM2.0 | CAM dice ^e | CAM docn ^f | 1984–1995 |

^a CSIM: Community Sea Ice Model.

^b POP: Parallel Ocean Program.

^c Prescribed sea ice concentrations (fractional cover) and thickness.

^d Prescribed climatological SSTs.

^e Prescribed sea ice concentrations.

^f Prescribed monthly SSTs.

tion by Bonan of the NCAR Land Surface Model (LSM), based on earlier work at NCAR and elsewhere (e.g., Bonan 1998). A “Common Land Model” was developed by Dai et al. (2003) to synthesize previous advances in land modeling and introduce new improvements. After initial testing by Zeng et al. (2002), it was incorporated into the Community Climate System Modeling framework (Blackmon et al. 2001) as the CLM2 with performance as described by Bonan et al. (2002).

A model consists of structure and data. Land processes are generally described at a local or plot scale whereas they communicate with the atmosphere of a climate model at the resolution of the atmospheric model (referred to as grid scale). Thus, the structure of CLM consists of local process rules together with rules for scaling from the plot scale to the grid scale. Data are included in the model either as universal constraints on processes or as tables correlated with the land cover description. Plot-scale processes are highly complex and studied by many scientific communities for many purposes. This complexity must be considerably simplified (i.e., in the sense of “dimensionality reduction”) to focus on the climate model’s more important objectives. These objectives are to determine land surface climate statistics and to simulate the interactions of land with the atmosphere on the grid scale. How best to link plot scale to the grid scale as well as how to best utilize current satellite data provided on an intermediate scale are complex issues of statistical modeling that are currently under active development.

Since Bonan et al. (2002), the CLM has been extensively scrutinized as a software package and in terms of its simulations. The land climate it simulates has substantially improved as a result of advances in (a) its process formulation and (b) its parent atmospheric model through better physics and higher resolution.

This report emphasizes a description of the CLM3’s contribution to climate simulations that include, in the full model, coupled oceans and sea ice [Oleson et al. (2004) provide a comprehensive documentation of the algorithms currently used by CLM].

2. Description of models and observational data used

As part of its support for the CCSM, NCAR carries out and archives a wide variety of climate simulations with current versions of CCSM. These are done either with the complete model or with various partial versions. For the latter, CLM can be integrated either with a prescribed atmosphere or with an interactive atmosphere but with prescribed sea surface temperatures (SSTs) and sea ice concentrations (fractional coverage). More is learned by comparisons of observations with ensembles of simulations than with a single simulation. Furthermore, if the ensemble members have distinct features, something may be learned about the roles of these features. Thus, we use an ensemble of simulations that are distinguished in terms of being the previous (CLM2) versus the current (CLM3) version of CLM, and in having prescribed or simulated SSTs, and in being of the old (T42) or new (T85) standard resolution of the parent atmospheric model [Community Atmosphere Model (CAM); Table 1].

Of the various process description changes made in advancing from CLM2 to CLM3, only two have been established to have noticeably changed the simulated climate. Both are largely the replacement of an algorithmically “defective” by a “satisfactory” treatment, rather than a fundamental advance in understanding of land processes. In particular, the conductance for transfer of sensible heat and moisture from soil to canopy air space was previously set to a constant that was intended

for dense vegetation but was a value much too small to be realistic for sparse vegetation; the net effect of this low conductance was that soil temperatures under sparse vegetation and heated by the sun become much too warm. This effect also substantially increased the surface air temperatures (up to several degrees or more) in semiarid regions. LSM previously suffered this problem less severely because it had adopted a larger constant conductance that had been inferred from observations involving less dense vegetation. The defective treatment in CLM had been adopted from the Biosphere–Atmosphere Transfer Scheme (BATS) as described in Dickinson et al. (1986). However, the latter was not similarly degraded because of its compensating unrealistic assumption of canopies always being opaque to solar radiation (Yang et al. 1999). A completely satisfactory treatment of undercanopy turbulent transport would involve more advanced micrometeorological modeling than is currently available. However, given the severity of the errors in simulation, we have tested various simpler fixes based on dimensional arguments that make the resistance depend on leaf and stem area index (LAI and SAI; Zeng et al. 2005), and implemented one in CLM3 (the effect of which is shown in Fig. 1a). The second such “improvement” involves a diagnostic 2-m temperature calculation that previously did not consistently include stability corrections and as a result under some conditions could generate biases of a few tenths of a degree in the diagnostic temperature estimation (Fig. 1b).

Early climate models were sufficiently inaccurate that surface air temperature observations could be compared with modeled soil or lowest model-level temperature, since the differences of several kelvins or more were within the accuracy attempted by the model. The diurnal cycle was usually ignored. In general, the logic of comparisons with observations requires reproducing in the model what is seen in the observation only to the accuracy expected from the model. The physical descriptions of land processes and their coupling to the atmosphere have become capable of providing temperatures over a grid square to an accuracy of about 1 K. Hence, a diagnostic surface air temperature is needed to that accuracy or better. Further accuracy in the provision of this temperature than attempted here may require a more accurate micrometeorological treatment of the timing and conditions under which the meteorological observations are currently made. Such corrections are expected to be less than 1 K.

The CLM3 has been much improved relative to CLM2 in various aspects of its code that allow more flexibility and efficiency in applications on a variety of high performance platforms. Of particular importance

are (a) optimum performance on both cache-dependent workstations and vector processor supercomputers, and (b) a subgrid-scale data structure in three levels. The internal data structures of the model were modified and the code was reorganized to achieve reasonable performance on two new vector architectures: the Earth Simulator in Japan and the Cray XI at Oak Ridge National Laboratory. This significant software engineering effort improved performance on both scalar/cache-based and vector platforms (1.8 times speedup on the IBM Power4 and 25.8 times speedup on the Cray X1). The code modifications for vectorization along with performance results are presented in Hoffman et al. (2005).

CLM, as its predecessor LSM, has included the idea of subgrid tiles that represent a histogram of the different forms of land cover within a grid square. These currently include lakes, glaciers, wetlands, and up to 16 standard land “plant functional types” (PFTs) that can include a “bare” soil. These surface types and their biophysical characteristics have not changed from that documented in Bonan et al. (2002). The tiling structure has now been extended to three levels in which grid cells are composed of multiple land units (e.g., glacier, lake, and vegetated), each of which can have snow columns, and the vegetated land units can have PFTs and soil columns. It is possible to distribute the PFTs over any of these levels, but for the sake of efficiency, this standard CLM has done this over the inner-level grid, which shares a common soil column. Except for different root profiles for different PFTs, no aspects of competition between PFTs are represented in the standard CLM.

Observational datasets for testing the model are the same as those used in Bonan et al. (2002). Monthly observed terrestrial air temperature and precipitation are provided by version 3.01 of the Willmott and Matsuura (2000) climatology covering the period 1950–96. Observed monthly snow depth was obtained from the global snow depth climatology of Foster and Davy (1988). Observed runoff was obtained from the University of New Hampshire–Global Runoff Data Center (UNH–GRDC) 0.5° monthly climatological composite runoff fields as inferred from river discharges (Fekete et al. 2000, 2002).

In addition, to help quantify the uncertainty in observations of temperature and precipitation, we employ several other datasets. For precipitation, we also use version 2 of the Global Precipitation Climatology Project (GPCP) dataset for 1979–2004 (Huffman et al. 1997; Adler et al. 2003), the Legates and Willmott climatology for 1920–80 (Legates and Willmott 1990a), the Precipitation Reconstruction over Land (PREC/L) clima-

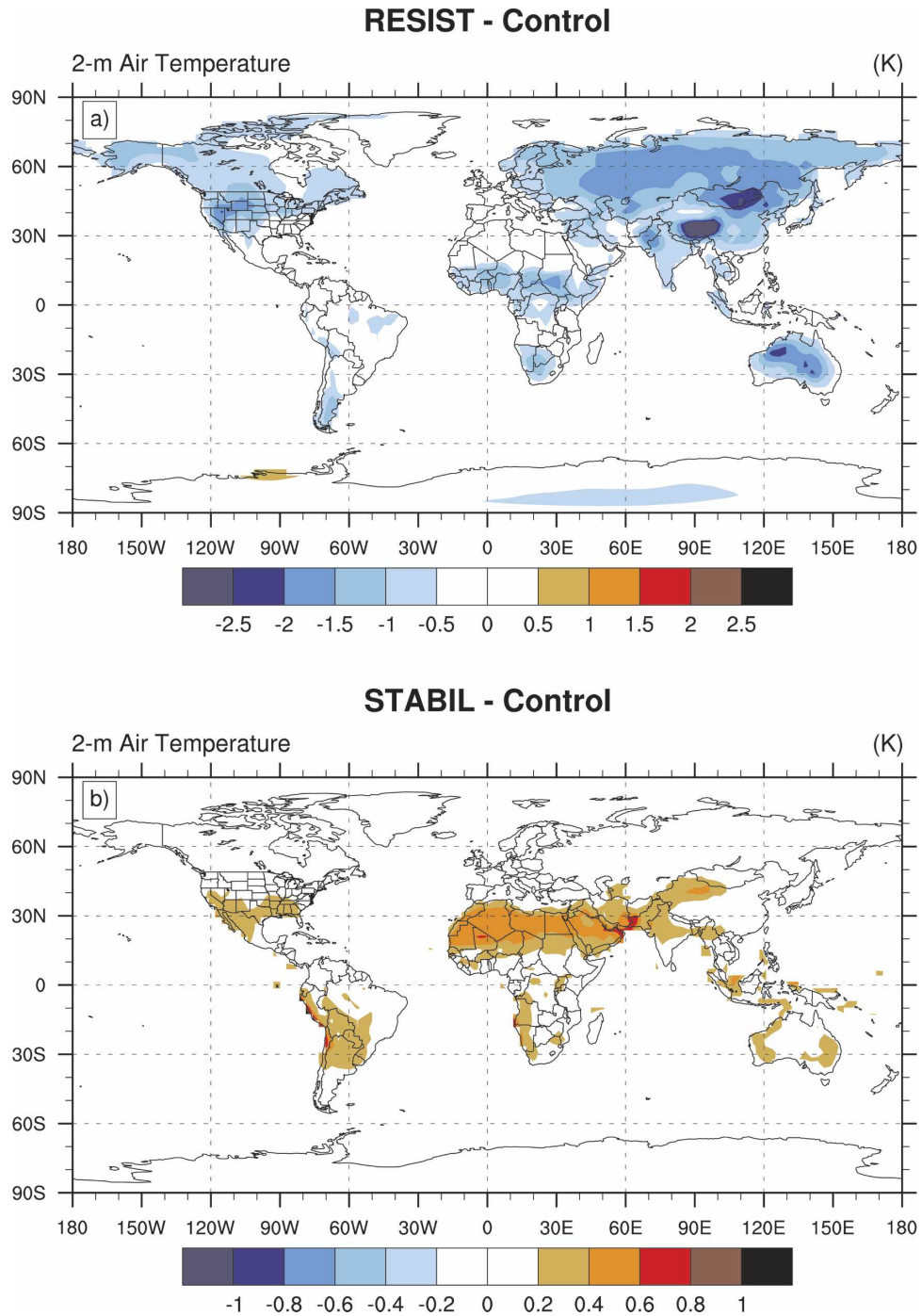


FIG. 1. (a) Differences in simulated annual 2-m air temperature (K) due to a change in the parameterization for resistance to transfer of sensible heat and moisture from soil to canopy air space (RESIST – Control) and (b) inclusion of consistent stability corrections (STABIL – Control), as described in the text. All three simulations were run with a version of CAM2/CLM2 for 22 yr with prescribed monthly SSTs (1979–2000). The first five years were discarded for spinup. “Control” in this figure only refers to the earlier CLM 2.0 version.

tology for 1948–2001 (Chen et al. 2002), the Climate Prediction Center (CPC) Merged Analysis of Precipitation (CMAP) climatology for 1979–98 (Xie and Arkin 1997), and the GXGXS dataset, which is a blend of multiple precipitation products for 1979–2000 (Large and Yeager 2004). Precipitation from the Tropical Rainfall Measuring Mission (TRMM) for 1998–2003 is also used for regions over the range of latitude 40°S – 40°N . Additional temperature datasets used are the Legates and Willmott climatology for 1920–80 (Legates and Willmott 1990b). All datasets are interpolated from their native resolution to T85. Regional averages are computed by applying the CCSM3.0_T85 land mask and fractional land to each dataset and applying area weighting.

3. Comparison of the land and near-surface atmospheric variables as simulated versus observed

a. Global comparisons

The 50-yr records of the simulations analyzed here are long enough to be useful for determination of year-to-year climate variability of land variables (e.g., Manabe and Stouffer 1996). Figure 2 shows the 50-yr record of land annual surface temperatures, precipitation, absorbed solar radiation, and downward longwave radiation of area- and time-weighted averages for the standard model and its low-resolution version, (CCSM3.0_T85 and CCSM3.0_T42). All the other state variables that are computed for land (not shown here), when similarly averaged, correlate to some degree with the temperature or precipitation records and have comparable levels of global variability. Such variability is expected to result from long-period variability of the coupled ocean–atmosphere element of the climate system as correlated to SSTs but will also include components of long-term “memory” related to land state variables. The larger excursions seen of $\pm 0.25\text{ K}$ and 0.1 mm day^{-1} are likely associated with large anomalies in tropical ocean SSTs (Koster et al. 2002; Reale and Dirmeyer 2002). However, attribution of “causes” of the land climate variability is not attempted here except as an approach to identify likely sources of biases in the land climatology that may result from biases in other components of the model. The correlations between surface radiative forcing and temperature are remarkably strong, more so for downward longwave radiation than for downward or absorbed solar radiation (Table 2). This strong correlation between downward longwave and surface temperatures is consistent with linkages between land and oceanic variability. The greater correlation of absorbed than incident solar radiation indicates a correlation of albedo with temperature as

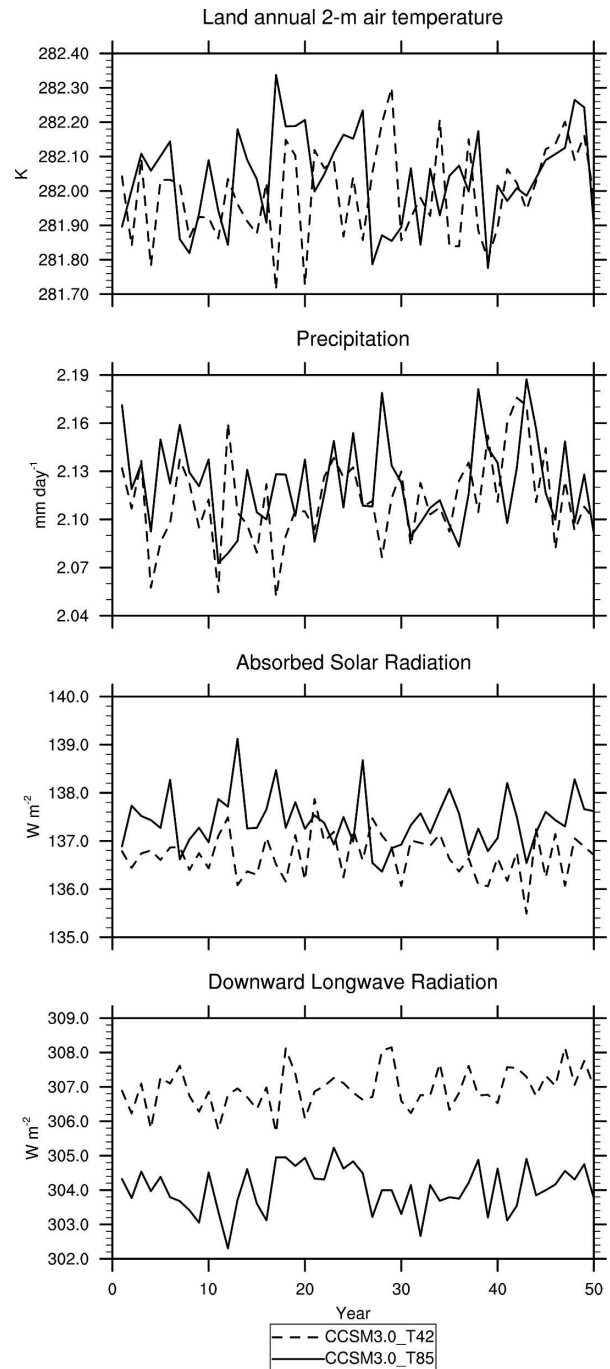


FIG. 2. Annual averages over global land of 2-m air temperature (K), precipitation (mm day^{-1}), absorbed solar radiation (W m^{-2}), and downward longwave radiation (W m^{-2}) for 50 yr of the CCSM3.0_T42 (years 601–650) and CCSM3.0_T85 (years 401–450) control simulations.

expected from snow albedo feedbacks (e.g., Hartmann 1994, p. 234). It may also be contributed to by regions of lower albedo having the strongest correlation between incident flux and temperature. The regression

TABLE 2. Linear correlations between annual global land 2-m air temperature and precipitation ($T'P'$), downward solar radiation ($T'SD'$), absorbed solar radiation ($T'SA'$), and downward longwave radiation ($T'LD'$). Here, r is the sample regression coefficient, and b is the slope of the regression line. The units for b are $\text{K} (\text{mm day}^{-1})^{-1}$ for $T'P'$, and $\text{K} (\text{W m}^{-2})^{-1}$ for $T'SD'$, $T'SA'$, and $T'LD'$. Results for the confidence level p are not shown for $p > 0.1$.

| | $T'P'$ | | | $T'SD'$ | | | $T'SA'$ | | | $T'LD'$ | | |
|-------------|--------|------|-----|---------|------|-------|---------|------|-------|---------|------|-------|
| | r | b | p | r | b | p | r | b | p | r | b | p |
| CCSM3.0_T85 | 0.00 | 0.00 | — | 0.38 | 0.08 | <0.01 | 0.51 | 0.12 | <0.01 | 0.72 | 0.15 | <0.01 |
| CCSM3.0_T42 | 0.21 | 1.03 | — | 0.19 | 0.04 | — | 0.39 | 0.11 | <0.01 | 0.83 | 0.19 | <0.01 |

coefficients in Table 2 quantify the connections between atmospheric radiative forcing and land air temperatures. In particular, an increase of net land radiation of $7\text{--}8 \text{ W m}^{-2}$ is associated with an increase in surface air temperatures of 1 K.

This correlation results from some combination of the temperature response to radiative forcing and radiative feedbacks resulting from temperature change. The latter involves changes in column temperature and water vapor profiles and cloud properties that change the downward radiation. The feedback from clear-sky downward longwave radiation is estimated to be approximately $2 \text{ W m}^{-2} \text{ K}^{-1}$, as would account for the difference between the solar and longwave regression coefficients.

The lack of correlation between global land tempera-

ture and precipitation is a consequence of multiple mechanisms of differing signs. In colder regions and those without water limitations (e.g., see Table 3), their increased water-holding capacities and increased evapotranspiration with higher temperature generally give positive such correlations whereas in warm but water-limited regions a reduction of evapotranspiration with reduction of precipitation can give a warmer surface and hence a negative correlation [e.g., June–August (JJA) in Table 5].

Figure 3 shows the annual cycle of global mean precipitation and temperature for a variety of observational datasets versus that obtained by the control simulation. Annual averages appear to be consistent with the observations. However, the modeled temperatures are somewhat high in winter. Although this bias may be

TABLE 3. Linear correlations between DJF high-latitude Northern Hemisphere land ($45^{\circ}\text{--}90^{\circ}\text{N}$, $0^{\circ}\text{--}360^{\circ}\text{E}$) 2-m air temperature and precipitation ($T'P'$), absorbed solar radiation ($T'SA'$), and downward longwave radiation ($T'LD'$), and downward longwave radiation with low clouds (LD'LC'), medium clouds (LD'MC'), high clouds (LD'HC'), and total clouds (LD'TC'). Here r is the sample regression coefficient, and b is the slope of the regression line. The units for b are $\text{K} (\text{mm day}^{-1})^{-1}$ for $T'P'$, $\text{K} (\text{W m}^{-2})^{-1}$ for $T'SA'$ and $T'LD'$, and $\text{W m}^{-2} (\% \text{ cloud})^{-1}$ for the cloud correlations. Results for the confidence level p are not shown for $p > 0.1$.

| | | Model | | | |
|---------|-----|-------------|-------------|---------------|-------------|
| | | CCSM3.0_T85 | CCSM3.0_T42 | CAM3/CLM3_T85 | CCSM2.0_T42 |
| $T'P'$ | r | 0.25 | 0.74 | 0.59 | 0.41 |
| | b | 3.62 | 13.64 | 7.41 | 7.47 |
| | p | 0.09 | <0.01 | <0.01 | <0.01 |
| $T'SA'$ | r | 0.06 | −0.36 | −0.38 | 0.20 |
| | b | 0.13 | −1.32 | −1.24 | 0.44 |
| | p | — | <0.01 | 0.02 | — |
| $T'LD'$ | r | 0.98 | 0.99 | 0.99 | 0.97 |
| | b | 0.25 | 0.25 | 0.24 | 0.26 |
| | p | <0.01 | <0.01 | <0.01 | <0.01 |
| LD'LC' | r | 0.57 | 0.61 | 0.62 | 0.20 |
| | b | 2.10 | 3.65 | 2.51 | 0.68 |
| | p | <0.01 | <0.01 | <0.01 | — |
| LD'MC' | r | −0.01 | 0.05 | 0.22 | −0.10 |
| | b | −0.06 | 0.26 | 1.07 | −0.41 |
| | p | — | — | — | — |
| LD'HC' | r | 0.27 | 0.59 | 0.63 | 0.40 |
| | b | 1.02 | 2.38 | 2.32 | 1.43 |
| | p | 0.06 | <0.01 | <0.01 | <0.01 |
| LD'TC' | r | 0.68 | 0.76 | 0.66 | 0.18 |
| | b | 2.83 | 4.83 | 2.73 | 0.77 |
| | p | <0.01 | <0.01 | <0.01 | — |

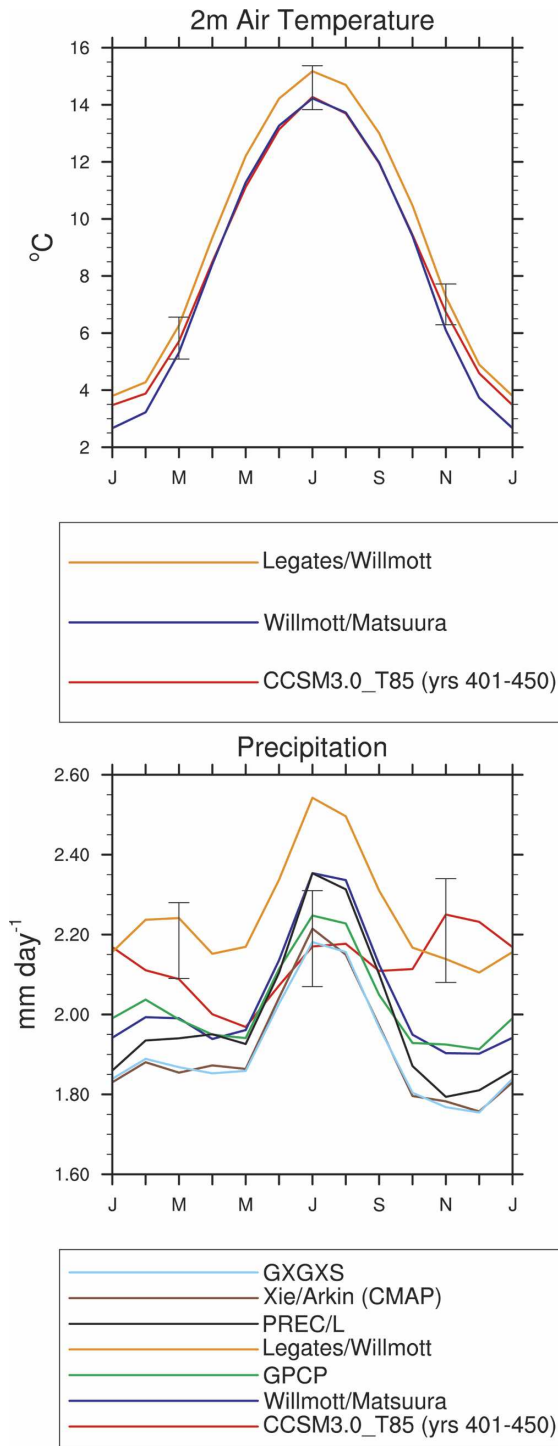


FIG. 3. Land seasonal cycle of 2-m air temperature ($^{\circ}\text{C}$) and precipitation (mm day^{-1}) over global land for the CCSM 3.0_T85 control compared to the various observational datasets, i.e., Willmott and Matsuura (2000), GPCP (Huffman et al. 1997; Adler et al. 2003), Legates and Willmott (1990a,b), PREC/L (Chen et al. 2002), CMAP (Xie and Arkin 1997), and GXGXS (Large and Yeager 2004). The bars with whiskers show the range of model simulations (Table 1) for March, July, and November.

within the noise level on the global mean, it derives mostly from larger anomalies from high latitudes in the Northern Hemisphere. The seasonal cycle of modeled precipitation also appears to be somewhat weaker than observed.

As the present study examines a land model as part of an integrated system, it is not possible to make direct comparisons with other land models alone. Various versions of the CLM have been extensively compared with local site data (e.g., Dai et al. 2003). Simulated surface fluxes of the coupled system can be compared to the Atmospheric Model Intercomparison Project (AMIP II) analysis of Henderson-Sellers et al. (2003). As this paper does not include a standard AMIP II simulation, a precise comparison is not possible. Their Fig. 3 shows, for global average, that the more recent models cluster around a ratio of sensible to latent heat in the range 0.55–0.75, with European Centre for Medium-Range Weather Forecasts (ECMWF) and National Centers for Environmental Prediction (NCEP)–NCAR reanalysis datasets on the low end of this range. The control of this study has a ratio of 0.68. Tropical sensible fluxes, for example, the Amazon, appear to be on the high side, possibly by as much as a factor of 2, relative to model consensus.

Bonan et al. (2002) described the major regional model biases found in CLM2/CAM2 at that time. To what extent do these biases persist, and how have they changed with advancement in the land and atmospheric model or by inclusion of an interactive ocean?

b. Northern high latitudes

Perhaps the most striking biases noted in Bonan et al. (2002) were at high northern latitudes in winter. Figure 4 compares December–February (DJF) for the standard model (CCSM3.0_T85) for surface air temperatures and precipitation with those observed north of 45°N . As in earlier models, high latitudes continue to show such a warm bias, in some regions, of over 10 K. As the region shown in Fig. 4 contains about one-fourth of the global land surface, an average anomaly of 4 K, approximately as seen, would bias the global average by 1 K. We consider further the large discrepancy seen in Alaska. We use all the model versions in ensemble form for the graphical comparison but quantify only the comparisons with the standard model version. The other versions, for the most part, agree better with this control than with the gridded observations.

Figures 5 and 6 compare the seasonal cycle of the Arctic Alaska and the remainder of Alaska, respectively, with the reference dataset. Also plotted are seasonal averages from Alaskan station tabulations, Barrow (north coast) and Bettles (on south side of Arctic

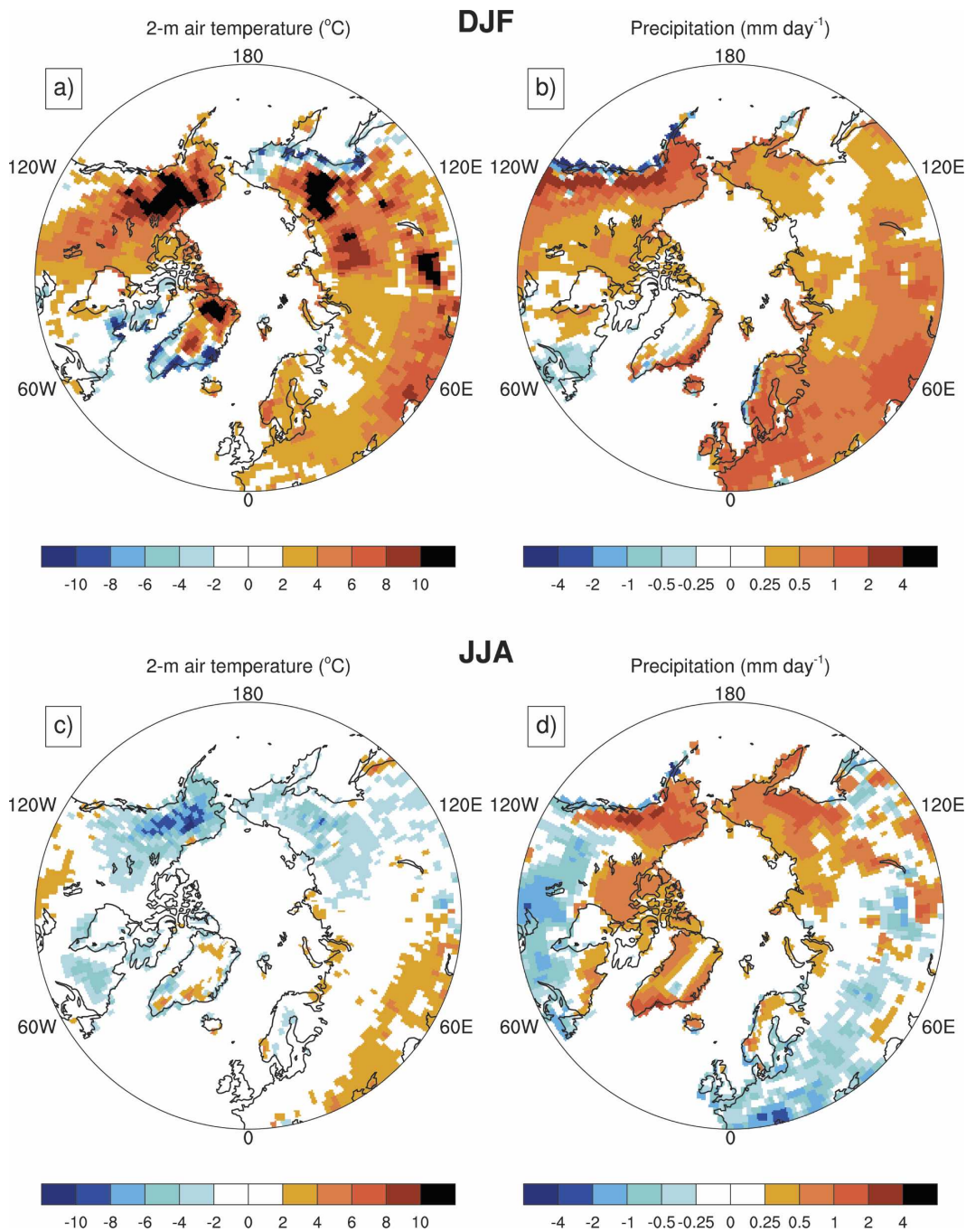


FIG. 4. The CCSM3.0_T85 2-m air temperature ($^{\circ}\text{C}$) and precipitation (mm day^{-1}) for Northern Hemisphere (45° – 90°N) (a), (b) winter (DJF average) and (c), (d) summer (JJA average) minus observations (Willmott and Matsuura 2000).

box), which bracket the Arctic region, and averages of Nome (east coast), Valdez (south coast), St. Paul (south coast), and Fairbanks in the middle of the lower Alaska box. The Arctic region is either 10 K too warm or 6 K too warm in winter depending on whether we believe the gridded comparison data or the station data. For the

rest of Alaska, the model in winter is either about 9 K too warm if compared only with the interior station (Fairbanks) or could be about right if coastal stations are given equal weight. Thus, it is possible that some of the disagreement would disappear if different choices were made in determining how to map the station data

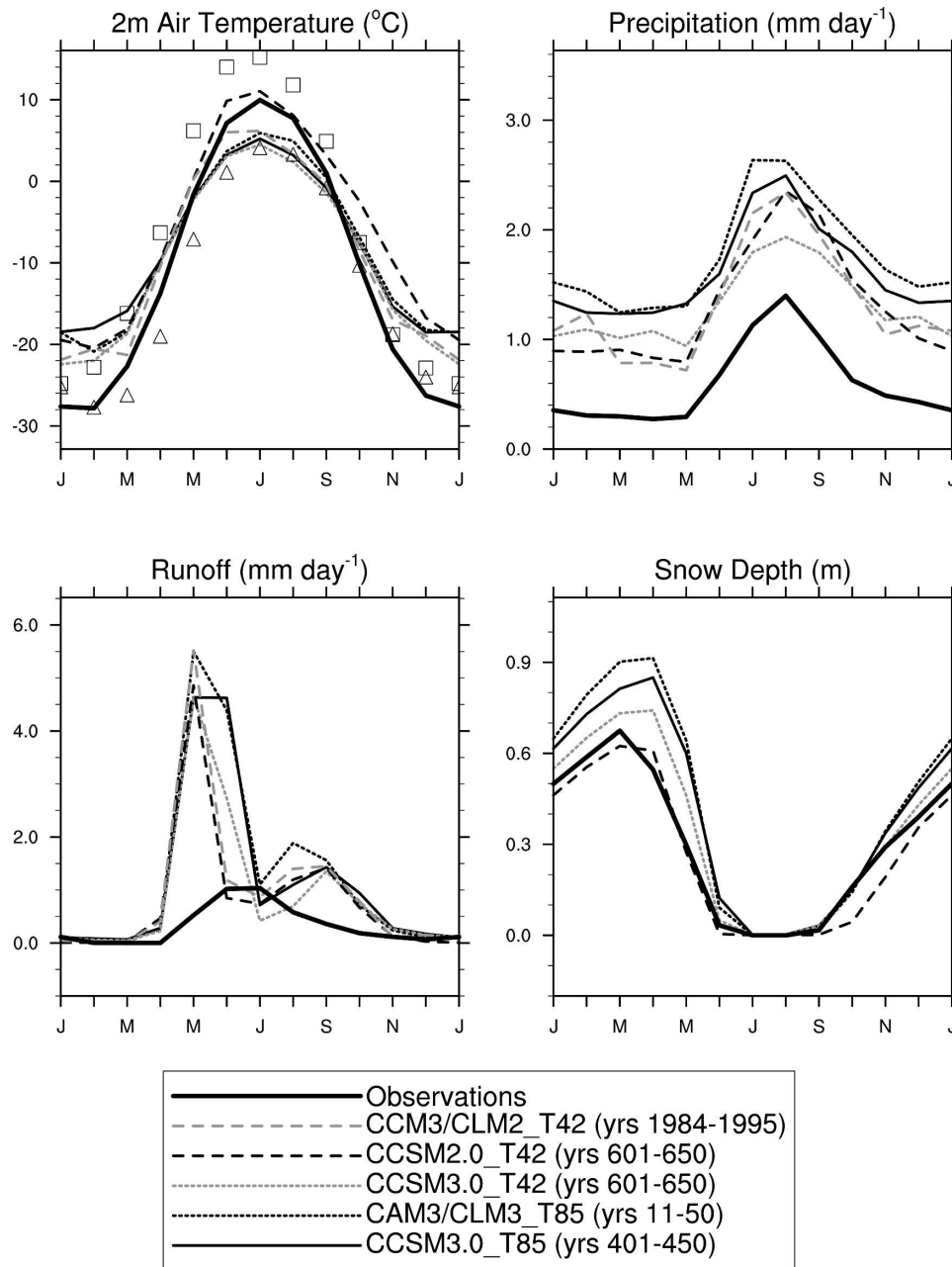


FIG. 5. Seasonal cycle of 2-m air temperature ($^{\circ}\text{C}$), precipitation (mm day^{-1}), total runoff (mm day^{-1}), and snow depth (m) compared to observations in the Alaskan Arctic ($66.5^{\circ}\text{--}72^{\circ}\text{N}$, $170^{\circ}\text{--}140^{\circ}\text{W}$) for the ensemble of simulations described in the text. Observations are from Willmott and Matsuura (2000; air temperature and precipitation), Fekete et al. (2002; runoff), and Foster and Davy (1988; snow depth). Model grid cells containing glaciers were masked out. Snow depth from CCM3/CLM2_T42 was not available. Also shown on the temperature plot are Barrow (triangles) and Bettles (squares) monthly station temperature data (obtained online at <http://www.climate-zone.com>).

to gridded data. The presence of large gradients not adequately resolved by the station data used to provide the gridded data may be a general difficulty in comparing simulated surface temperatures for regions containing extensive coastlines such as Alaska. The model

shows a factor-of-2 overprediction of the Alaskan winter precipitation. Snowfall is notoriously difficult to measure, but the inference of a model excess is supported by the comparable excess in model-versus-measured runoff and snow depth. Some of the snow

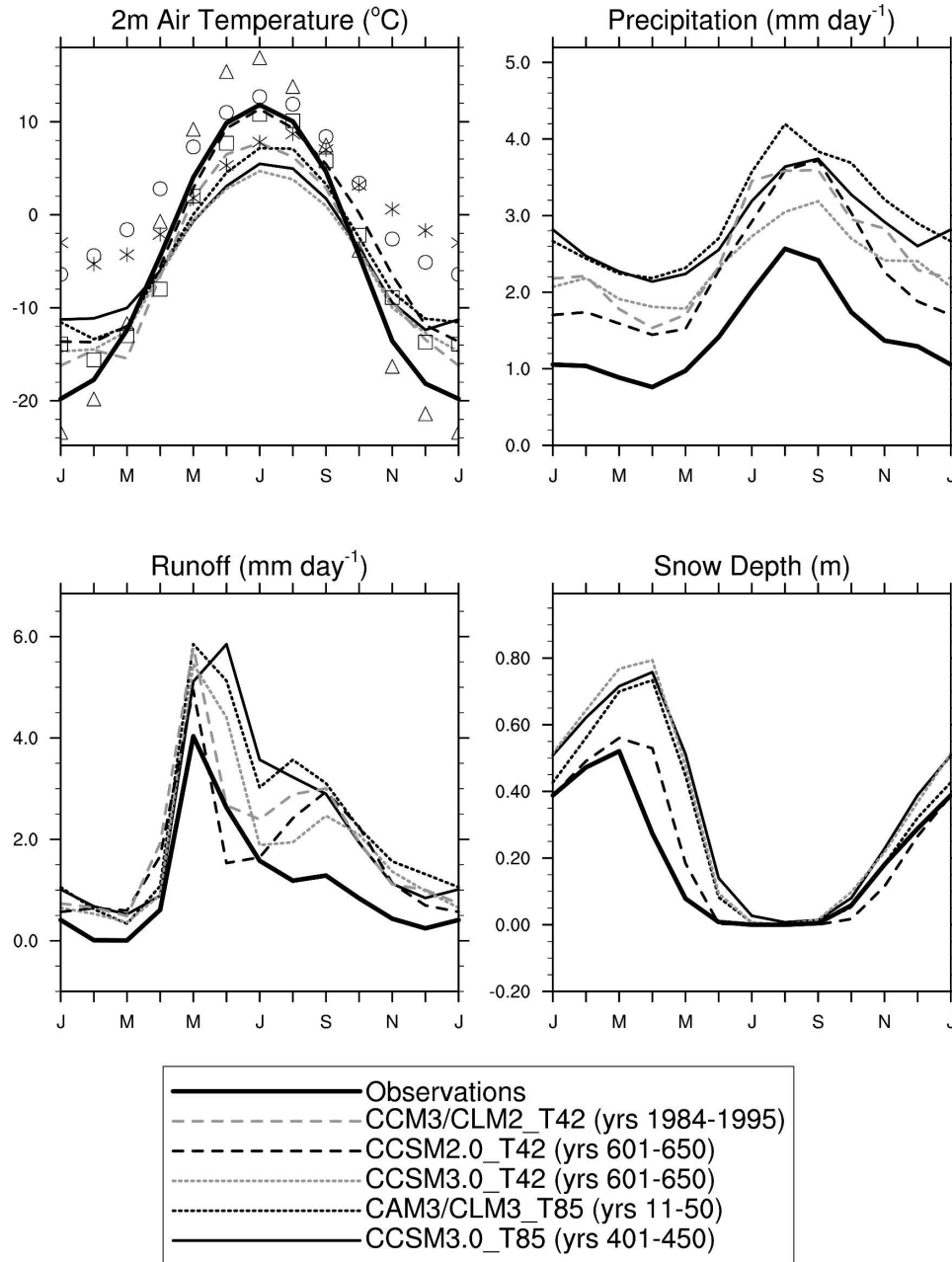


FIG. 6. Same as in Fig. 5, but for Alaska. Station data are for (59° – 66.5°N , 170° – 140°W) Fairbanks (triangles), Nome (squares), Valdez (circles), and St. Paul (asterisks).

depth excess is also attributable to the model's neglect of sublimation of blowing snow, which would reduce the snow depth by at least 0.03 m (Bowling et al. 2004).

In the Alaskan Arctic summer, the "data" appear to be an average of the interior Bettles and coastal Barrow temperatures, whereas the model is not much warmer than coastal Barrow. Thus, although the model in summer in the Alaskan Arctic is evidently too cold by a few degrees, exactly how much may be difficult to judge. In

the lower Alaska box, the average of coastal and interior station temperatures in summer is about equal to the value of the data. On the other hand, the modeled temperatures (Fig. 6) are about 2–3 K colder than the coldest coastal station (St. Paul) such that simulated summer is colder by at least 5 K compared to both the station average and the data. This summer coolness appears to be connected to an excessively active hydrological cycle all year round. The snow season lasts up to

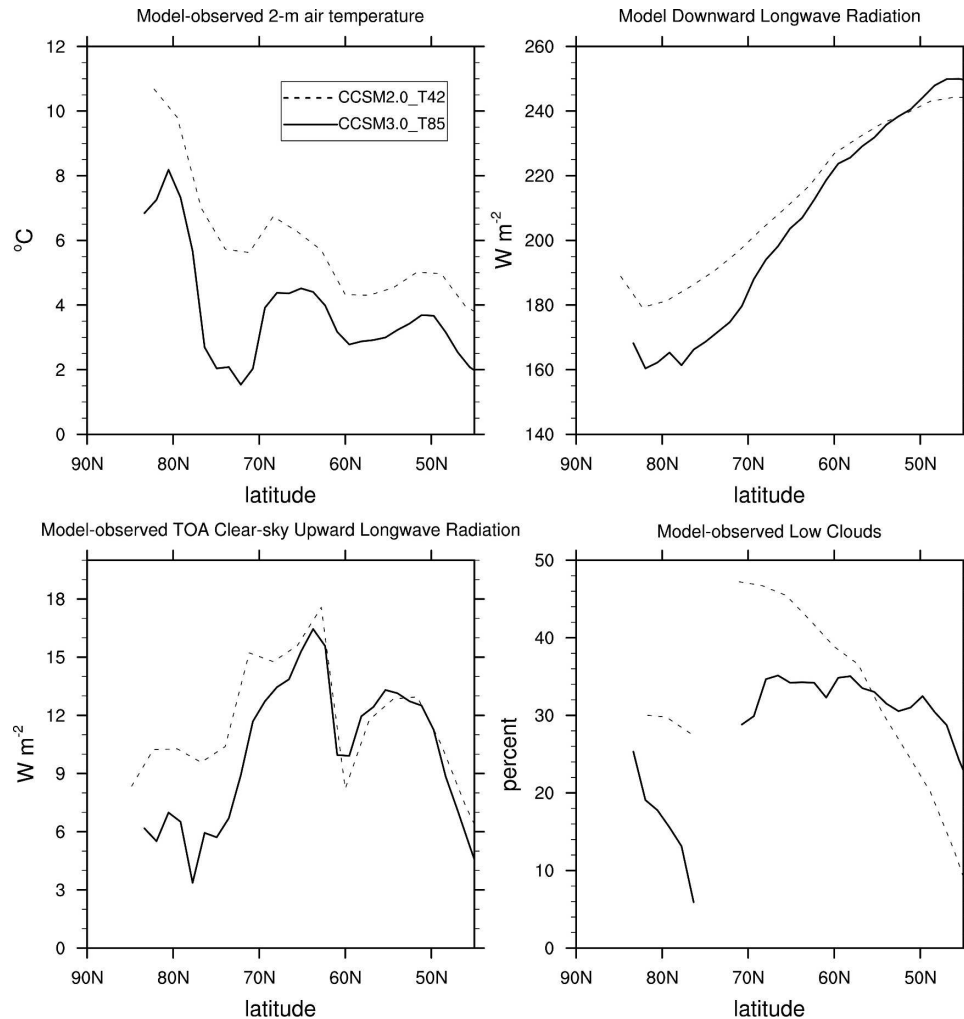


FIG. 7. Zonal averages of differences between models (CCSM2.0_T42 and CCSM3.0_T85) and observations of land 2-m air temperature ($^{\circ}C$), downward longwave radiation (models only; $W m^{-2}$), top of the atmosphere clear-sky upward longwave radiation ($W m^{-2}$), and low clouds (percent). Observations are from Willmott and Matsuura (2000; air temperature), the Earth Radiation Budget Experiment (ERBE; TOA clear-sky upward longwave radiation), and Hahn et al. (1988; low clouds). To account for missing data in the observed low-cloud climatology, only the model grid cells that had corresponding valid observed values were incorporated into the zonal mean.

several months longer than observed, and even after the snow disappears, the soil remains close to saturated, and overall the low clouds also appear to be excessive compared to those from the ISCCP D2 data (not shown; e.g., Rossow and Schiffer 1999). The ISCCP flux down (FD) (Zhang et al. 2004) estimation of incident solar radiation for this box in summer (not shown) exceeds by about $100 W m^{-2}$ that which is provided by the model.

The year-to-year variability of the winter air temperatures for land poleward of $45^{\circ}N$ is almost perfectly (0.98–0.99) correlated with the variability of the down-

ward longwave radiation (Table 3). This correlation indicates that a $1 W m^{-2}$ increase in downward longwave radiation corresponds to about a $0.25-K$ increase in air temperature. As some of the change in downward longwave radiation is likely positive feedback (possibly as much as half), this correlation coefficient is regarded as providing an upper limit to the radiative forcing needed to change surface temperatures by a given amount. Consequently, modeling the observed temperatures may require a reduction in downward longwave radiation that is approximately $10 W m^{-2}$.

Decreases of precipitation also correlate with de-

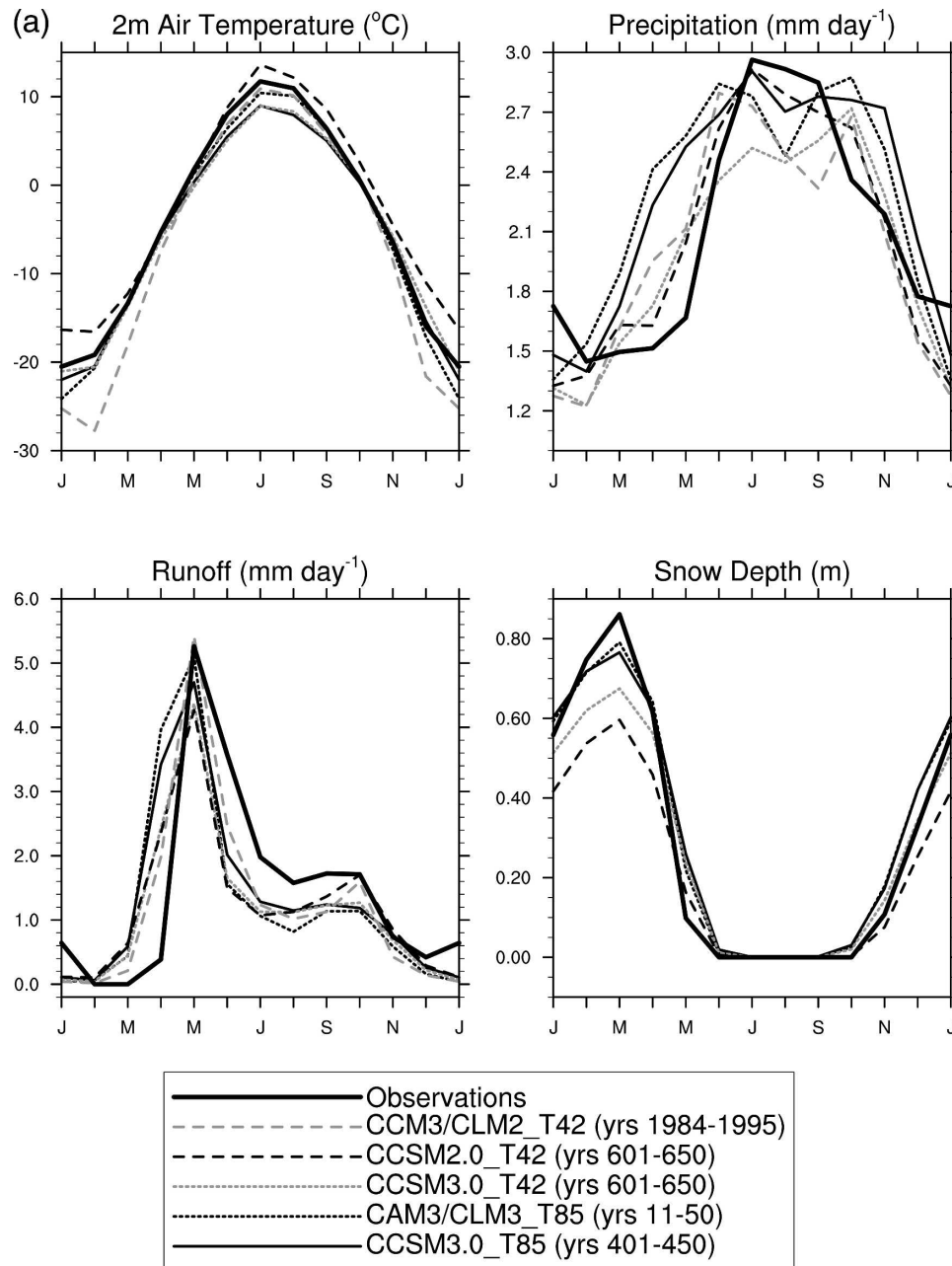


FIG. 8. Seasonal cycle of 2-m air temperature ($^{\circ}\text{C}$), precipitation (mm day^{-1}), total runoff (mm day^{-1}), and snow depth (m) compared to observations in (a) eastern Canada (50° – 60°N , 80° – 55°W), (b) northern Europe (60° – 70°N , 5° – 45°E), and (c) eastern Siberia (50° – 66.5°N , 90° – 140°E) for the ensemble of simulations described in the text. Observations are from Willmott and Matsuura (2000; air temperature and precipitation), Fekete et al. (2002; runoff), and Foster and Davy (1988; snow depth). Model grid cells containing glaciers were masked out. Snow depth was not available from CCM3/CLM2_T42.

creases of air temperature, presumably in part because of the decreased capacity of the atmosphere to hold water. The warm bias is significantly less than in the previous version of the model (Fig. 7). The downward longwave radiation has also been reduced in approximate agreement with the above inferred sensitivity pa-

rameter. This reduction appears to have been caused largely by a reduction in low clouds although they may still be in excess (Fig. 7). The excess low clouds and high surface temperatures appear to indicate that modeled downward longwave is still too large.

Several minor flaws in the land model may also ex-

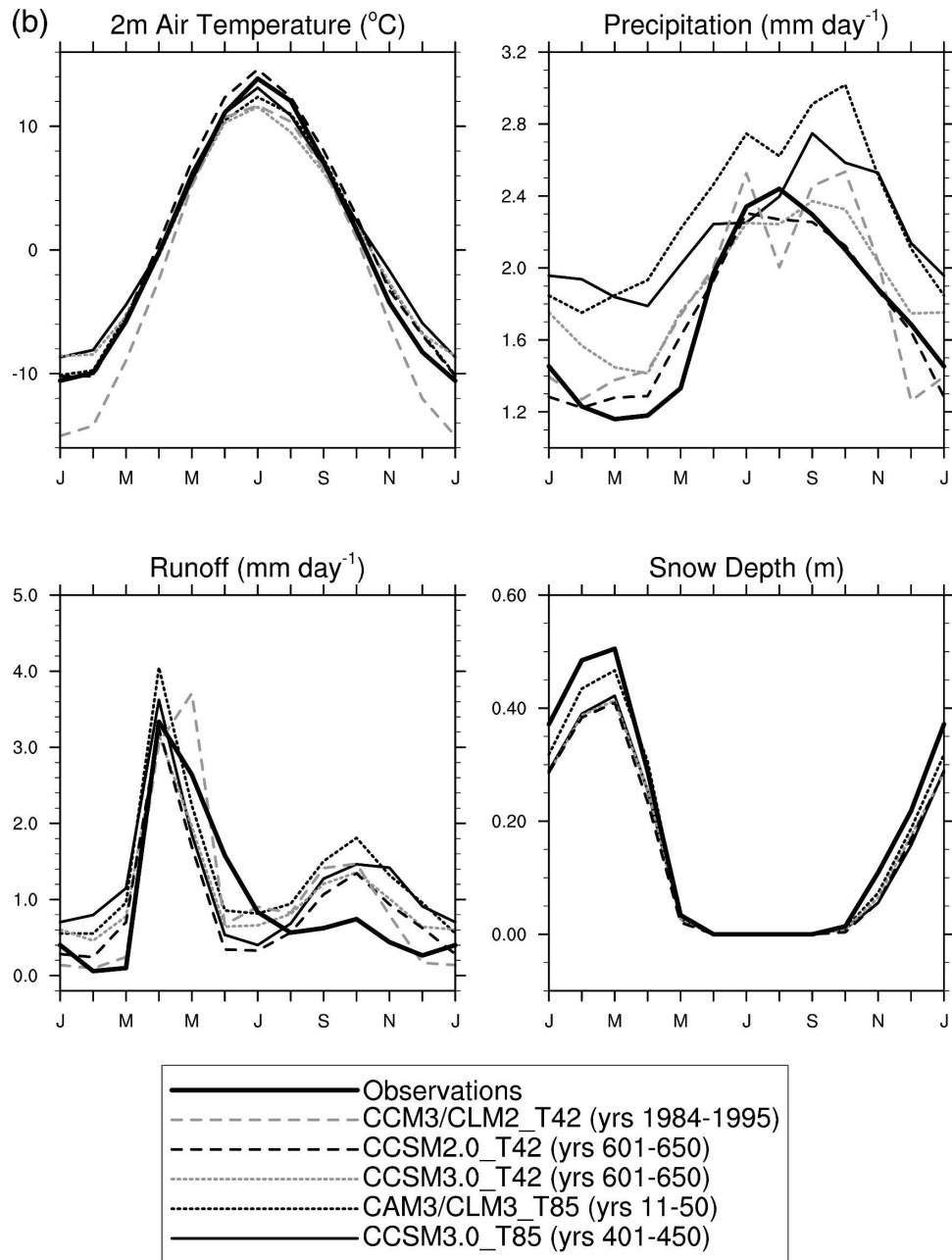


FIG. 8. (Continued)

plain some of the bias. In particular, an erroneously low value was used for snow emissivity, that is, a value of 0.97, in disagreement with a more appropriate value of 0.99, for example, as obtained by Dozier and Warren (1982) for hemispheric emissivity. Also of concern are the differences in determining the 2-m temperature in the model compared to the observational procedures. The model calculates it as a 24-h average of the temperature above the vegetation (e.g., forests), whereas it is measured as the average of daily maximum and mini-

mum temperatures in a clearing. For stable winter conditions, the modeled temperature is expected to have a high bias from this difference. Also, inaccuracies in estimation of fractional snow cover may bias the albedo low, leading to warmer temperatures equatorward of polar night.

Figure 8a shows that the overall climatological disagreements for the eastern Canada box are less than for Alaska. The control with interactive ocean is cold in summer by 2–3 K, but the temperature of CLM3 with

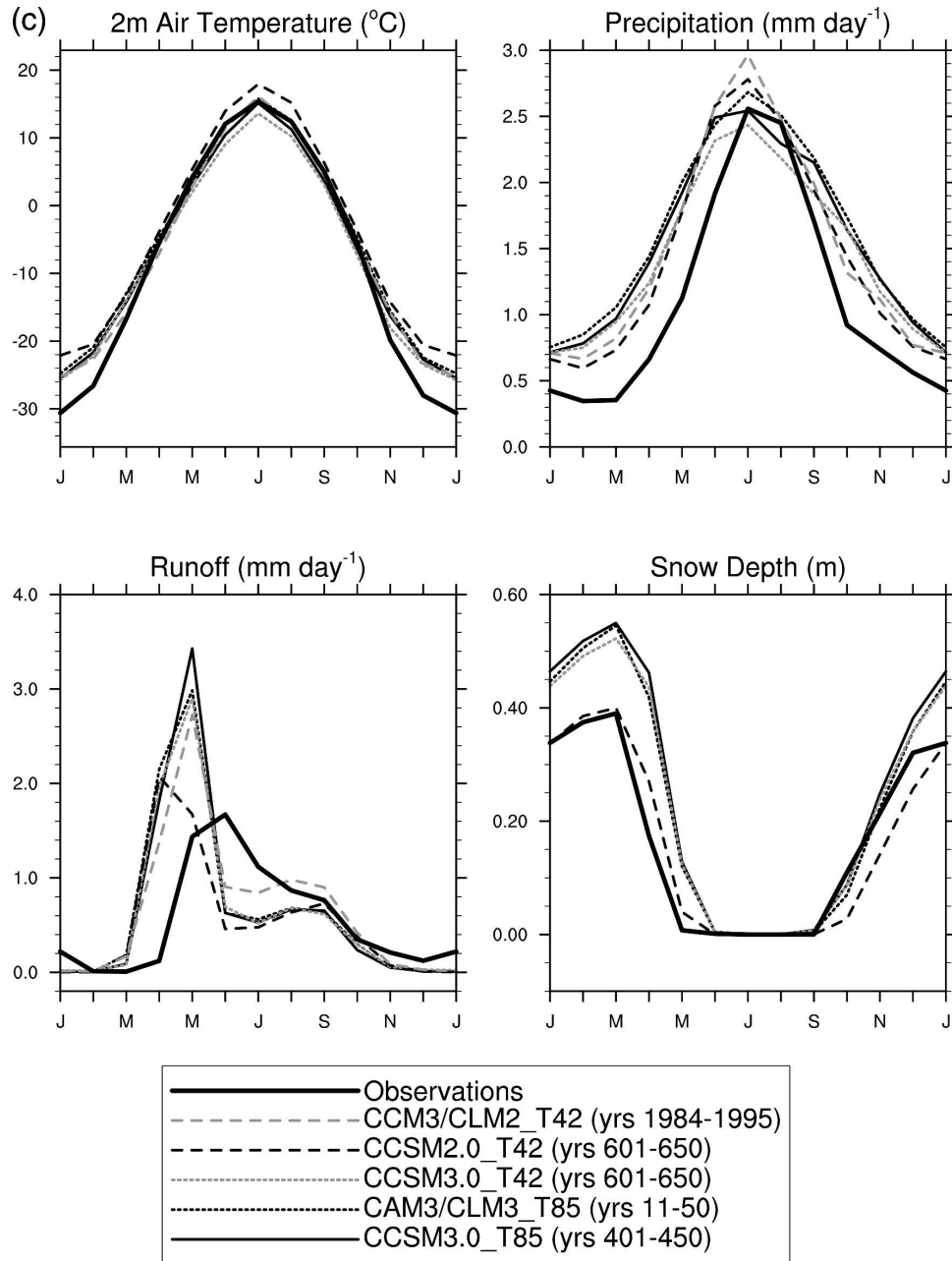


FIG. 8. (Continued)

the same resolution but with prescribed SSTs is close to that observed. The control precipitation is too high in spring. However, snow depth is within the accuracy of the observations, and the difference between observed and modeled runoff is consistent within the probable accuracy of the observations. Figure 8b shows northern Europe as another area of reasonable agreement, and Fig. 8c shows that eastern Siberia appears to be too warm in winter but in very good agreement with observations in other seasons. Its hydrological cycle appears

to be too active and the peak runoff occurs too early, likely in part resulting from too early a snowmelt. The concentration of winter warm anomalies around Alaska and Siberia (Fig. 4a) is consistent with differences (not shown) between simulated and observed winds in the lower troposphere. In particular, where the warmest anomalies occur, the modeled 850-mb winds are anomalously southerly by $3\text{--}5\text{ m s}^{-1}$ and where temperatures are less in disagreement, winds are anomalously northerly by about the same amount.

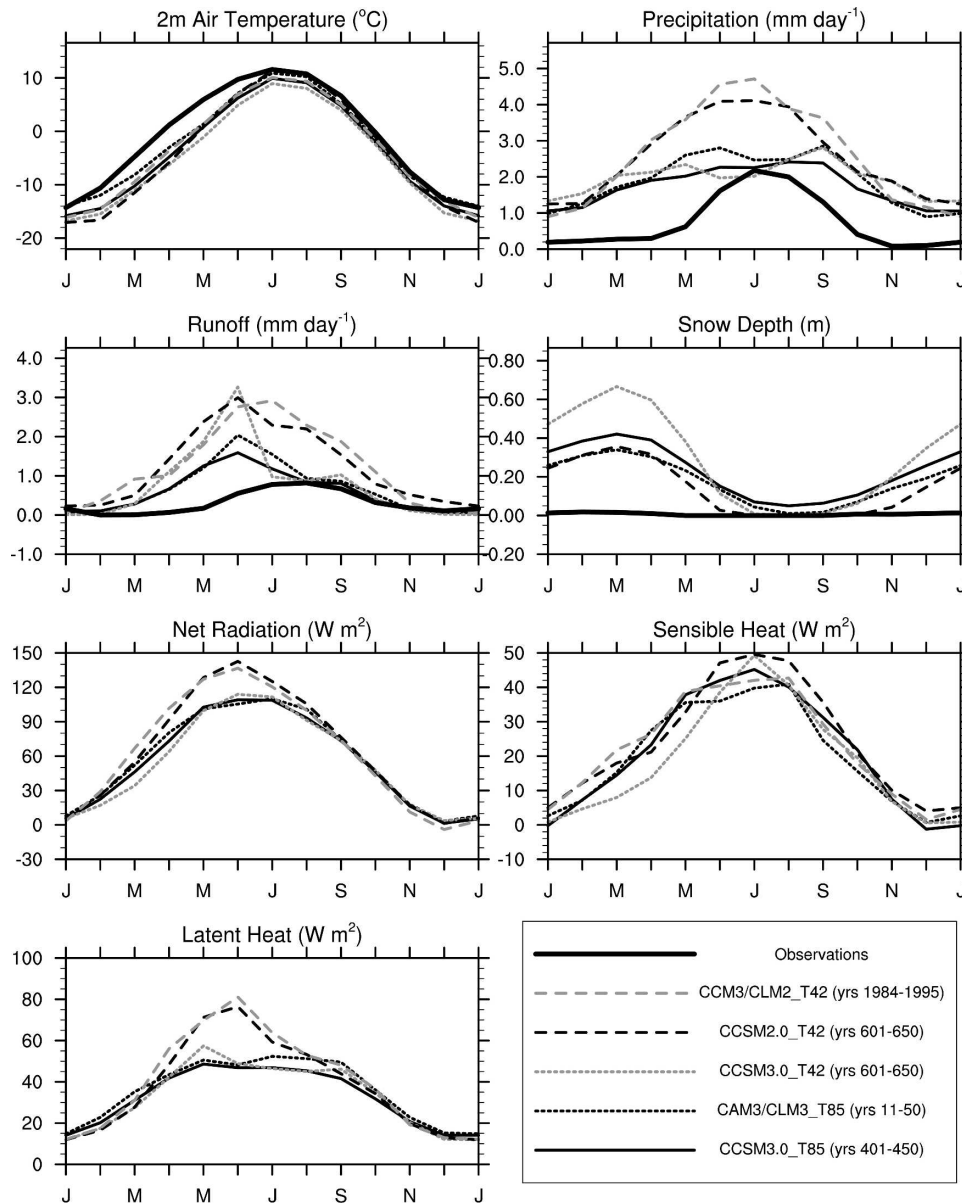


FIG. 9. Seasonal cycle of 2-m air temperature ($^{\circ}\text{C}$), precipitation (mm day^{-1}), total runoff (mm day^{-1}), snow depth (m), net radiation (W m^{-2}), and sensible and latent heat (W m^{-2}) in the Tibetan Plateau ($30^{\circ}\text{--}40^{\circ}\text{N}$, $80^{\circ}\text{--}100^{\circ}\text{E}$) for the ensemble of simulations described in the text. Model grid cells containing glaciers were masked out. Snow depth was not available from CCM3/CLM2_T42.

In conclusion, simulation biases in high-latitude winters are sufficient to have a significant impact on the global average land climatology. In this region and season, surface temperature variability is very highly correlated with downward longwave. Excessive low clouds promote an excess in this downward longwave radiation. This excess warms the surface and the warmer surface promotes excess precipitation, snowpack, and runoff. The largest anomalies occur when the surface temperatures are further increased by anomalously

southerly winds, but where winds are too northerly, the excess downward longwave is compensated. Summers are too cold in high latitudes, apparently because of reduction of solar radiation by excess of clouds and probably also contributed to by the excess of winter snowpack.

c. Over Tibet

Figure 9 shows the simulated net radiation, sensible and latent heat fluxes, air temperature, precipitation,

runoff, and snow accumulation over Tibet for the various model versions. The observations are uncertain because of the need to apply elevation corrections to the mapped temperatures and the apparent sparseness of the data. The air temperature of the control model appears to be substantially colder than the gridded observations only in spring. However, several other lines of evidence indicate a summer season that is somewhat too cold. Various authors have recently estimated some of the modeled quantities through remote sensing or by modeling coupled with observations. In particular, Oku and Ishikawa (2004) provide a thermal-imagery-based estimation of annual-diurnal variation of skin temperature from the Geostationary Meteorological Satellite (GMS). Skin temperature has a stronger diurnal range than air temperature, but skin and air temperature tend to be reasonably close averaged over a 24-h period. Their data support winter temperatures, if anything, a few degrees colder than indicated, as measured in Fig. 9. They also support early spring temperatures closer to that modeled. However, they also indicate that there are about six months when the skin temperature is so in excess of freezing that very little snow could be present, again suggesting that the modeled summer could be too cold. This bias may be a result of too-extensive cloudiness and a consequent underestimation of net radiation by the model [the latter supported by surface observations reported by Gao et al. (2004)].

Considering the substantial spatial variability and large diurnal variability of temperature over Tibet as indicated by Oku and Ishikawa (2004) and Wen and Su (2003), it may not be possible to achieve much better agreement with temperature observations than shown here. However, the modeled hydrological cycle is likely too active. In particular, the annual runoff is at least twice that estimated by observations. The observational estimates of precipitation and of runoff could both be low by as much as a factor of 2 in midsummer, but their peak cannot be off by more than a month. The modeled wintertime precipitation is about 1 mm day^{-1} , whereas the observations indicate 0.2 mm day^{-1} . Evidently, the model is producing much more winter and spring snowfall than would be realistic. Although as shown by the plotted latent flux, about two-thirds of the snowfall is sublimated, the remaining snowpack still exceeds that measured by an order of magnitude and, consequently, the spring runoff is far in excess of that observed. Several other observational datasets were examined for consistency (i.e., those referenced in the legend of Fig. 3). They show that the observational datasets bracket to some extent the magnitude of the precipitation peak during summer, but all show the CLM precipitation to

be far too high in other months. They are, however, likely to all be based on much the same station data.

The lower-tropospheric circulation anomalies mentioned in the previous section are connected to a Siberia high shifted too far eastward and a westerly wind anomaly to the east of Tibet that would advect relatively moist air. The unrealistic precipitation may also be contributed by inadequate model resolution or from problems with the formulation of atmospheric and land processes in the complex terrain. The summer temperature cold anomaly appears to result from the excessive snow lasting into the summer, but it may also occur from an inadequate treatment of the complex terrain, its interaction with snow dynamics, and their joint determination of springtime albedos. The albedo of Tibet in winter as measured by the Moderate Resolution Imaging Spectroradiometer (MODIS) is much less than expected for a snow surface, supporting the surface measurements of nearly no snowpack. Considerable snow, however, could have blown into low areas shaded from satellite view. In any case, the observed overall low surface albedos in winter would support a much more rapid warming and melting of whatever snow had accumulated than would the high albedos of flat snow surfaces provided by the model. Flanner and Zender (2005) have shown that including penetration of solar radiation into the snowpack can reduce its depth and increase surface temperatures.

d. Africa

Figure 10 shows the annual average difference over Africa between modeled and observed air temperatures, downward longwave radiation, total precipitable water, and downward solar radiation. The surface air over North Africa is cold in the model by several degrees. The current surface radiation formulation may introduce a small cold bias. In particular, the unrealistic high value of surface emissivity, that is, 0.96 versus observed closer to 0.90 (Ogawa and Schmugge 2004) may account for a few tenths of a degree (Zhou et al. 2003). Although the modeled albedo in the Sahel may be somewhat high, and in the Sahara somewhat low (Oleson et al. 2003; Wang et al. 2004), the Clouds and the Earth's Radiant Energy System (CERES) shortwave cloud forcing indicates that the overall impact of this term is small.

There is a pronounced negative anomaly in the downward longwave flux over North Africa (Fig. 10b as estimated by the ISCCP FD product) that is consistent with an overlying atmosphere that is too cold and dry and so provides too little downward longwave to the surface. Solar fluxes are in better agreement with observations (Fig. 10d). The model-simulated total pre-

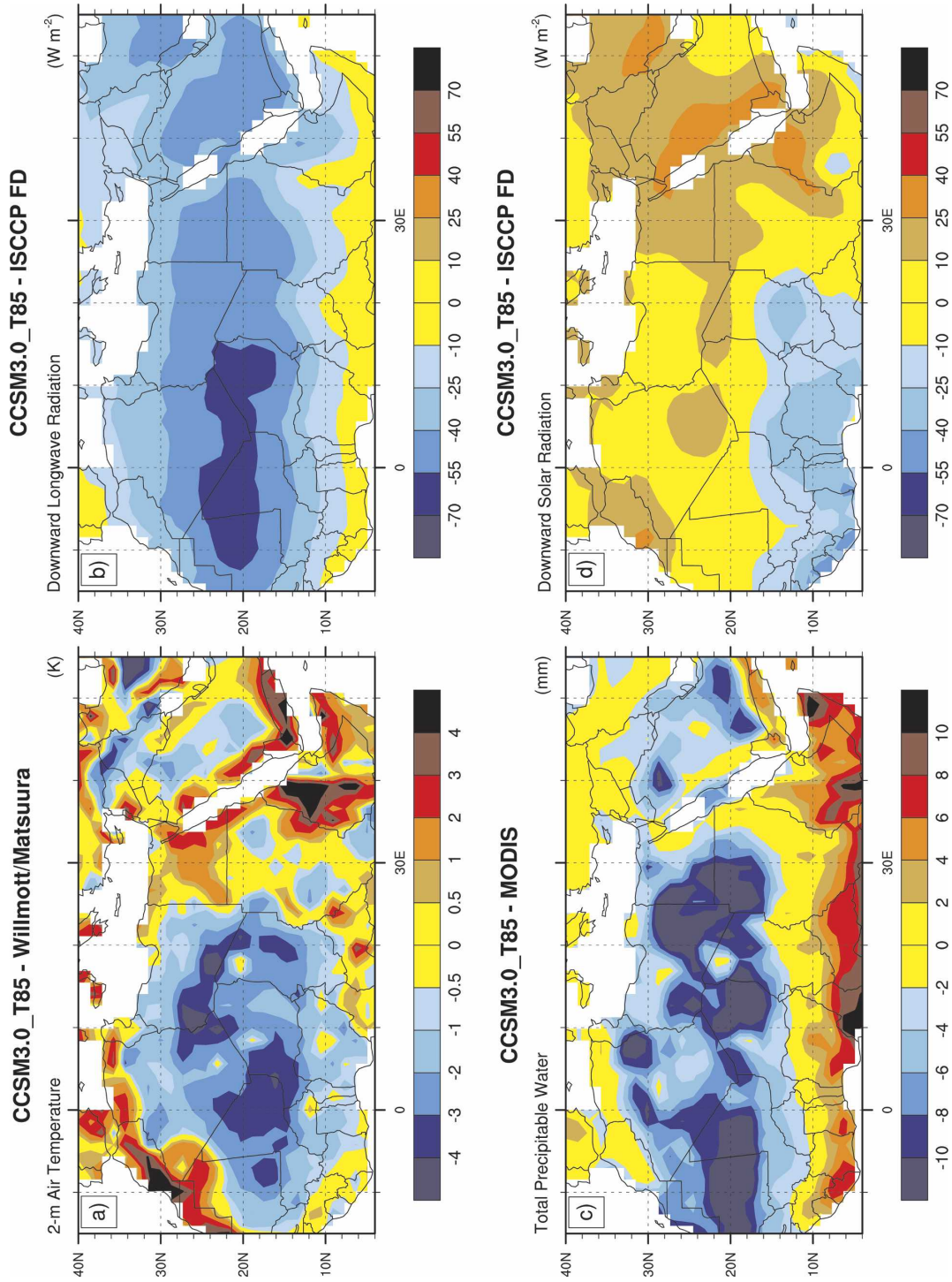


FIG. 10. CCSM3.0_T85 annual (a) 2-m air temperature (K), (b) downward longwave radiation ($W m^{-2}$), (c) total precipitable water (mm), and (d) downward solar radiation ($W m^{-2}$) for North Africa compared to observations. Observations are from Willmott and Matsuura (2000; air temperature), ISCCP FD (Zhang et al. 2004; longwave and solar radiation), and MODIS (total precipitable water).

TABLE 4. Linear correlations between annual land 2-m air temperature and downward longwave radiation ($T'LD'$), and downward longwave radiation and total precipitable water ($LD'TPW'$) for the Sahara Desert (16° – 30° N, 20° W– 30° E). Here r is the sample regression coefficient, and b is the slope of the regression line. The units for b are $\text{K} (\text{W m}^{-2})^{-1}$ for $T'LD'$ and $\text{W m}^{-2} \text{mm}^{-1}$ for $LD'TPW'$.

| Model | $T'LD'$ | | | $LD'TPW'$ | | |
|---------------|---------|------|-------|-----------|------|-------|
| | r | b | p | r | b | p |
| CCSM3.0_T85 | 0.67 | 0.12 | <0.01 | 0.75 | 3.27 | <0.01 |
| CCSM3.0_T42 | 0.71 | 0.14 | <0.01 | 0.71 | 3.04 | <0.01 |
| CAM3/CLM3_T85 | 0.71 | 0.11 | <0.01 | 0.79 | 3.18 | <0.01 |
| CCSM2.0_T42 | 0.70 | 0.12 | <0.01 | 0.76 | 3.10 | <0.01 |

precipitable water (TPW) is low by about 8 mm compared to that given by MODIS (Fig. 10c). A similar but not quite-so-strong difference is seen in comparison with ECMWF and NCEP–NCAR reanalyses (not shown).

Table 4 shows correlations between annual mean air temperature, downward longwave radiation, and total precipitable water for the Sahara Desert region. Temperature is strongly correlated with downward longwave radiation and TPW in all models. The tabulated regression coefficients associate a deficit in TPW of 8 mm with a 26 W m^{-2} deficit in downward longwave and temperatures cold by 3 K. These estimates are in agreement with the observed temperature deficit, but corre-

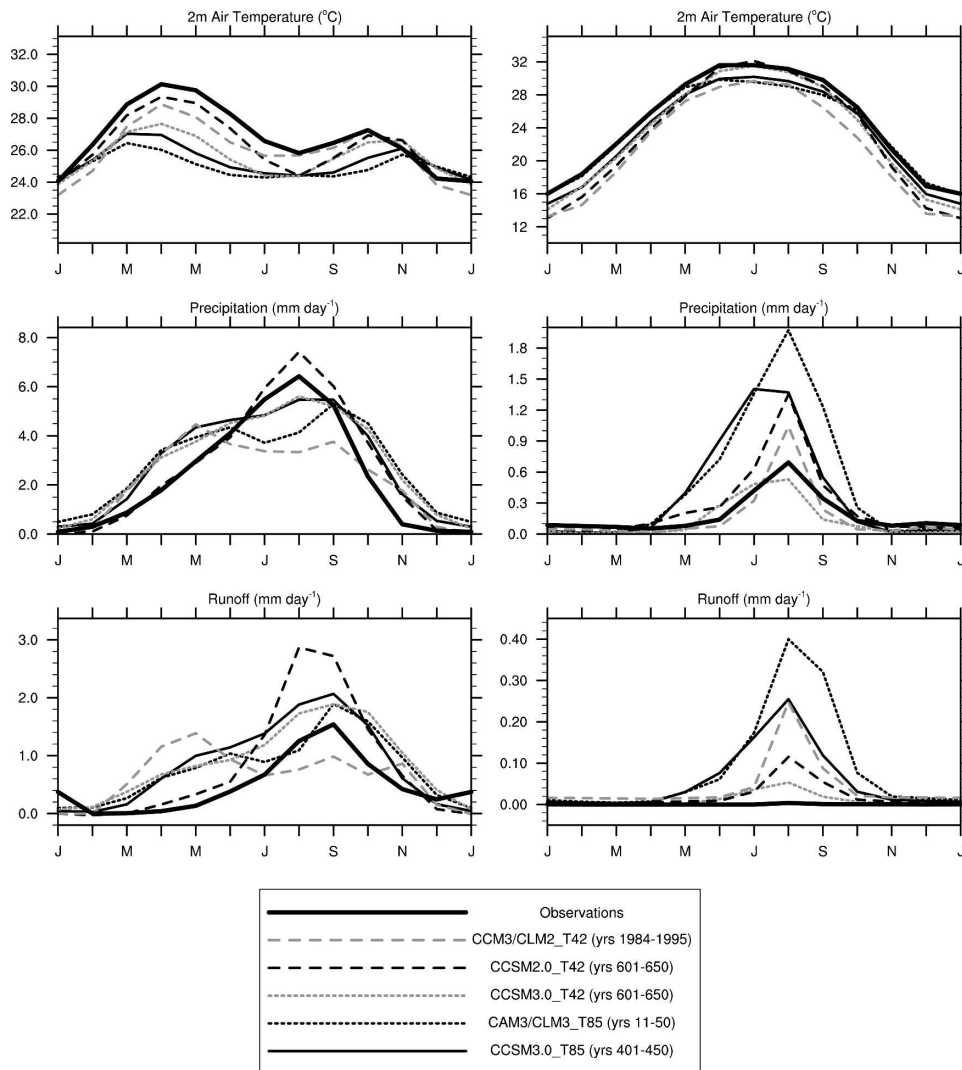


FIG. 11. Seasonal cycle of 2-m air temperature ($^{\circ}\text{C}$), precipitation (mm day^{-1}), and total runoff (mm day^{-1}) in (left column) the Sahel (6° – 16° N, 5° W– 15° E) and (right column) the Sahara Desert (16° – 30° N, 20° W– 30° E) regions for the ensemble of simulations described in the text.

respond to a downward longwave deficit less than that seen in Fig. 10b. This Fig. 10b estimate of downward longwave flux is most likely to be in error, since it is obtained by more indirect means than the TPW or the temperatures. The deficit of TPW is less in the Sahel, but reinforced by a negative bias in the downward solar radiation (Fig. 10d) coupled with slightly high albedos (Oleson et al. 2003; Wang et al. 2004) that may also contribute to the cold bias.

Figure 11 compares the seasonal cycle of surface air temperature, precipitation, and runoff over the Sahel and Sahara for all the model versions with that observed. The cold temperature anomaly over the Sahel was increased in moving from CLM2 to CLM3, and higher resolution also makes it slightly worse. Precipitation appears reasonable except for a springtime excess that may be connected to the peak in the cold temperature anomaly at that time, while runoff is overestimated in most months. Over the Sahara, the temperature anomaly has improved in midwinter to better match the observed values but has worsened in summer relative to that observed and compared to some of the other model runs. Summer precipitation is considerably higher than observed and becomes more so with higher resolution. The model also continues to have a problem (not shown) with a large excess of precipitation over the Arabian Peninsula.

e. Northern South America

The Amazon basin is biased warm and dry in most months, and runoff is overall low compared to observations (Figs. 12 and 13). Annual precipitation is underestimated by about 16%, but disagreements are more pronounced in the wet season. The model wet season starts a month or two earlier but does not have nearly as strong a peak as observed. Biases in runoff follow the precipitation biases (annual runoff is only about half of that observed).

The largest warm biases occur in the July through September dry season and are associated with a large deficit of evapotranspiration accompanying a strong depletion of soil moisture. The Amazon forests, however, are known to continue to transpire through the dry season, and only pastures show such a deficit (Matsuyama 1992; Fu and Li 2004; Shuttleworth 1988; Malhi et al. 2002; Nepstad et al. 2002). Annual evaporation of intercepted water in CCSM3.0_T85 is 34% of rainfall, about double that expected (Shuttleworth 1988; Ubarana 1996; Marin et al. 2000). Also, 64% of rainfall is returned to the atmosphere by evapotranspiration, which compares with observational estimates that are closer to 50% (Shuttleworth 1988; Matsuyama 1992; Malhi et al. 2002). The excess canopy evaporation is

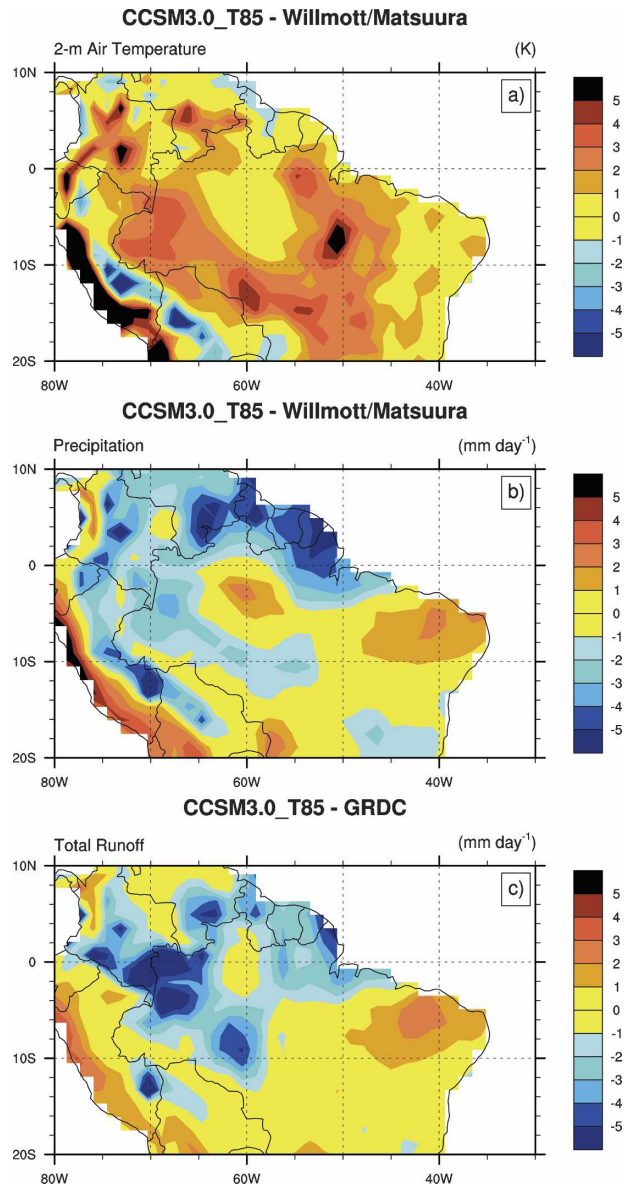


FIG. 12. CCSM3.0_T85 annual (a) 2-m air temperature (K), (b) precipitation (mm day^{-1}), and (c) total runoff (mm day^{-1}) for northern South America compared to observations. Observations are from Willmott and Matsuura (2000; air temperature and precipitation) and Fekete et al. (2002; runoff).

eliminated in CLM versions under development that provide more realistic downscaling to the fractional areas and intensities of the actual precipitation. Elimination of the deficit in runoff and the excessive drying may require an atmospheric model that provides more realistic amounts of precipitation and improvements in CLM's treatment of soil water (e.g., Nepstad et al. 1994), and perhaps also its modeling of transpiration (Dai et al. 2004).

The temperature, precipitation, and runoff biases

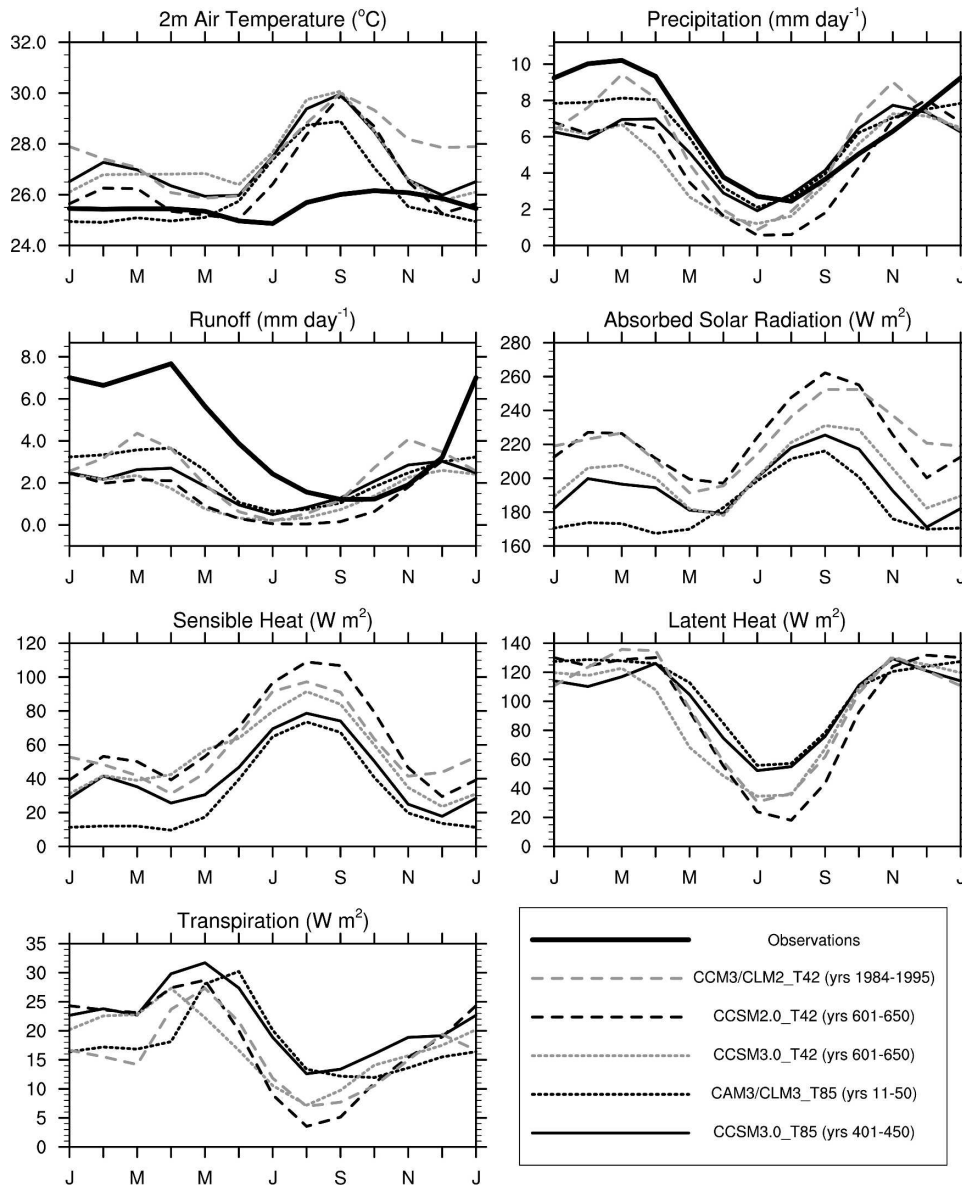


FIG. 13. Seasonal cycle of 2-m air temperature ($^{\circ}\text{C}$), precipitation (mm day^{-1}), total runoff (mm day^{-1}), absorbed solar radiation (W m^{-2}), sensible and latent heat (W m^{-2}), and transpiration (W m^{-2}) in Amazonia (10°S – 0° , 70° – 50°W) for the ensemble of simulations described in the text.

have been somewhat amplified in most months by inclusion of the ocean component of CCSM3.0_T85 compared to those seen with prescribed SSTs (CAM3/CLM3_T85). This amplification is connected to an increase of the incidence of solar radiation. Table 5 shows the year-to-year DJF and JJA correlations between 2-m temperature versus precipitation and downward solar and longwave radiation. The correlations with both radiative terms are positive, except that the downward longwave correlation becomes insignificant for the uncoupled simulation. The precipitation correlations are

strongly negative except for the DJF uncoupled simulation. The correlations suggest the temperatures could be 1 K less if precipitation were increased by about 1 mm day^{-1} or absorbed solar reduced by about 10 W m^{-2} .

4. Conclusions and discussion

This paper analyzes the land climatologies of simulations by the recent publicly released CCSM 3.0. Its control is at T85 resolution and includes an interactive ocean. This is compared with various observational

TABLE 5. Linear correlations between DJF and JJA Amazonia (10°S–0°, 70°–50°W) 2-m air temperature and precipitation ($T'P'$), absorbed solar radiation ($T'SA'$), and downward longwave radiation ($T'LD'$). Here r is the sample regression coefficient, and b is the slope of the regression line. The units for b are K (mm day⁻¹)⁻¹ for $T'P'$ and K (W m⁻²)⁻¹ for $T'SA'$ and $T'LD'$. Results for the confidence level p are not shown for $p > 0.1$.

| | | DJF | | | |
|---------|-----|-------------|-------------|---------------|-------------|
| | | CCSM3.0_T85 | CCSM3.0_T42 | CAM3/CLM3_T85 | CCSM2.0_T42 |
| $T'P'$ | r | -0.84 | -0.82 | -0.17 | -0.91 |
| | b | -0.93 | -0.82 | -0.15 | -0.75 |
| | p | <0.01 | <0.01 | — | <0.01 |
| $T'SA'$ | r | 0.91 | 0.81 | 0.69 | 0.88 |
| | b | 0.09 | 0.08 | 0.03 | 0.08 |
| | p | <0.01 | <0.01 | <0.01 | <0.01 |
| $T'LD'$ | r | 0.72 | 0.71 | 0.16 | 0.56 |
| | b | 0.26 | 0.19 | 0.03 | 0.19 |
| | p | <0.01 | <0.01 | — | <0.01 |
| | | JJA | | | |
| $T'P'$ | r | -0.82 | -0.72 | -0.71 | -0.26 |
| | b | -1.14 | -1.46 | -1.06 | -0.57 |
| | p | <0.01 | <0.01 | <0.01 | 0.07 |
| $T'SA'$ | r | 0.71 | 0.47 | 0.74 | 0.19 |
| | b | 0.10 | 0.06 | 0.09 | 0.03 |
| | p | <0.01 | <0.01 | <0.01 | — |
| $T'LD'$ | r | 0.33 | 0.30 | 0.05 | 0.52 |
| | b | 0.08 | 0.06 | 0.01 | 0.05 |
| | p | 0.02 | 0.04 | — | <0.01 |

datasets and with other simulations that either have lower resolution, or prescribed SSTs, or are earlier versions of the model. These analyses emphasize simulation of the standard climatological surface air temperature and precipitation. The overall impression gained is that the higher resolution and recent improvements have improved simulations over land, but that some regions and seasons have slightly deteriorated or remain problematical.

The most detailed examinations are of such regions that are currently regarded as especially problematical; these are, in particular, high northern latitudes in winter, northern Africa, Tibet, and the Amazon. The excessively warm temperatures of high latitudes in winter appear connected to a modeled excess of low clouds and consequent excess of downward longwave radiation. Its longitudinal variation is consistent with an anomaly in low-level circulation. A cold bias in temperature over North Africa is consistent with a deficit in the overlying column water vapor, and hence a deficit in the downward longwave radiation. Since the two continental-scale areas of multidegree temperature modeling errors are primarily attributable to errors in downward longwave radiation from deficiencies in the atmospheric simulation, it may be concluded that further improvements in the land model alone can at best provide modest improvements to the comparisons between modeled and observed surface temperatures.

The winter warm anomalies that persist into the

spring through the melt season may be comparably influenced by deficiencies in the parameterizations of snow cover and its interactions with vegetation. The potential for use of improved satellite datasets for constraining various vegetation properties to change simulated temperatures by as much as about 1 K is demonstrated by Tian et al. (2004a,b). In particular, they demonstrated improvement in the summer high-latitude cold biases, and the Amazon dry season warm bias. If soil albedos and emissivity were better represented in arid and semiarid regions (Oleson et al. 2003; Zhou et al. 2003) again order of 1-K differences would be realized.

The simulated climate of Tibet appears to have a large excess of precipitation, especially outside the summertime peak. Its excessive snow persists far too long into summer and reduces surface temperatures. Such deficiencies may result from various inadequacies in the atmospheric model's treatment of the moist atmospheric processes in the presence of this complex lower boundary, or from deficiencies in circulation. The excess persistence of the snow may also be contributed to by the neglect of sublimation of blowing snow and by albedos that are excessive in the presence of snow compared to observations.

The Amazon simulation suffers from inadequate precipitation relative to that observed in most months, and from a very dry surface during the dry season. The latter is a response in part to the deficit in precipitation

but is probably exacerbated by deficiencies in the current treatments of canopy interception, soil water storage, runoff, and transpiration. Improvements in these treatments are expected to somewhat alleviate but not remove the underestimations of precipitation and runoff. Strong negative correlations of seasonal precipitation with temperature may be coupled with oceanic variability, especially during the rainy season, when no such correlation is found for prescribed SSTs.

Acknowledgments. This study is based on model integrations that were performed by NCAR and CRIEPI with support and facilities provided by NSF, DOE, MEXT, and ESC/JAMSTEC. The authors have been supported by their contributions to this paper by NSF and DOE, in part through grants, NSF- ATM-03433485 and DOE - DE-FG02-01ER63198. We thank Ann Henderson-Sellers and an anonymous reviewer for their helpful suggestions.

REFERENCES

- Adler, R. F., and Coauthors, 2003: The Version-2 Global Precipitation Climatology Project (GPCP) monthly precipitation analysis (1979–present). *J. Hydrometeor.*, **4**, 1147–1167.
- Blackmon, M., and Coauthors, 2001: The Community Climate System Model. *Bull. Amer. Meteor. Soc.*, **82**, 2357–2376.
- Bonan, G. B., 1998: The land surface climatology of the NCAR Land Surface Model coupled to the NCAR Community Climate Model. *J. Climate*, **11**, 1307–1326.
- , K. W. Oleson, M. Vertenstein, S. Levis, X. Zeng, Y. Dai, R. E. Dickinson, and Z.-L. Yang, 2002: The land surface climatology of the Community Land Model coupled to the NCAR Community Climate Model. *J. Climate*, **15**, 3123–3149.
- Bowling, L. C., J. W. Pomeroy, and D. P. Lettenmaier, 2004: Parameterization of blowing-snow sublimation in a macroscale hydrology model. *J. Hydrometeor.*, **5**, 745–762.
- Chen, M., P. Xie, and J. E. Janowiak, 2002: Global land precipitation: A 50-yr monthly analysis based on gauge observations. *J. Hydrometeor.*, **3**, 249–266.
- Dai, Y., and Coauthors, 2003: The Common Land Model. *Bull. Amer. Meteor. Soc.*, **84**, 1013–1023.
- , R. E. Dickinson, and Y.-P. Wang, 2004: A two-big-leaf model for canopy temperature, photosynthesis, and stomatal conductance. *J. Climate*, **17**, 2281–2299.
- Dickinson, R. E., A. Henderson-Sellers, P. J. Kennedy, and M. F. Wilson, 1986: Biosphere-Atmosphere Transfer Scheme (BATS) for the NCAR Community Climate Model. NCAR Tech. Note TN-275+STR, 72 pp.
- Dozier, J., and S. G. Warren, 1982: Effect of viewing angle on the infrared brightness temperature of snow. *Water Resour. Res.*, **18**, 1424–1434.
- Fekete, B. M., C. J. Vorosmarty, and W. Grabs, cited 2000: Global composite runoff fields based on observed river discharge and simulated water balances. [Available online at <http://www.grdc.sr.unh.edu/>]
- , —, and —, 2002: High-resolution fields of global runoff combining observed river discharge and simulated water balances. *Global Biogeochem. Cycles*, **16**, 1042, doi:10.1029/1999GB001254.
- Flanner, M. G., and C. S. Zender, 2005: Snowpack radiative heating: Influence on Tibetan Plateau climate. *Geophys. Res. Lett.*, **32**, L06501, doi:10.1029/2004GL022076.
- Foster, D. J., Jr., and R. D. Davy, 1988: Global snow depth climatology. USAF Environmental Technical Applications Center Tech. Note USAFETAC TN-88 (006), 48 pp.
- Fu, R., and W. Li, 2004: The influence of the land surface on the transition from dry to wet season in Amazonia. *Theor. Appl. Climatol.*, **78**, 97–110.
- Gao, Z., N. Chae, J. Kim, J. Hong, T. Choi, and H. Lee, 2004: Modeling of surface energy partitioning, surface temperature, and soil wetness in the Tibetan prairie using the Simple Biosphere Model 2 (SiB2). *J. Geophys. Res.*, **109**, D06102, doi:10.1029/2003JD004089.
- Hahn, C. J., S. G. Warren, J. London, R. L. Jenne, and R. M. Chervin, 1988: Climatological data for clouds over the globe from surface observations. Rep. NDP026, Carbon Dioxide Information Analysis Center, Oak Ridge National Laboratory, Oak Ridge, TN, 54 pp.
- Hartmann, D. L., 1994: *Global Physical Climatology*. Academic Press, 234 pp.
- Henderson-Sellers, A., P. Irannejad, K. McGuiffie, and A. J. Pitman, 2003: Predicting land-surface climates—Better skill or moving targets? *Geophys. Res. Lett.*, **30**, 1777, doi:10.1029/2003GL017387.
- Hoffman, F., M. Vertenstein, H. Kitabata, and J. White III, 2005: Vectorizing the Community Land Model (CLM). *Int. J. High Perform. Comput. Appl.*, **19**, 247–260.
- Houghton, J. T., Y. Ding, D. J. Griggs, M. Noguer, P. J. van der Linden, X. Dai, K. Maskell, and C. A. Johnson, Eds., 2001: *Climate Change 2001: The Scientific Basis*. Cambridge University Press, 944 pp.
- Huffman, G. J., R. F. Adler, A. Chang, R. Ferraro, A. Gruber, A. McNab, B. Rudolf, and U. Schneider, 1997: The Global Precipitation Climatology Project (GPCP) combined precipitation dataset. *Bull. Amer. Meteor. Soc.*, **78**, 5–20.
- Koster, R. D., P. A. Dirmeyer, A. N. Hahmann, R. Ijpelaar, L. Tyahla, P. Cox, and M. J. Suarez, 2002: Comparing the degree of land–atmosphere interaction in four atmospheric general circulation models. *J. Hydrometeor.*, **3**, 363–375.
- Large, W. G., and S. G. Yeager, 2004: Diurnal to decadal global forcing for ocean and sea-ice models: The data sets and flux climatologies. NCAR Tech. Note NCAR/TN-460+STR, 111 pp.
- Legates, D. R., and C. J. Willmott, 1990a: Mean seasonal and spatial variability in gauge-corrected, global precipitation. *Int. J. Climatol.*, **10**, 111–127.
- , and —, 1990b: Mean seasonal and spatial variability in global surface air temperature. *Theor. Appl. Climatol.*, **41**, 11–21.
- Malhi, Y., E. Pegoraro, A. D. Nobre, G. P. Pereira, J. Grace, A. D. Culf, and R. Clement, 2002: Energy and water dynamics of a central Amazonian rain forest. *J. Geophys. Res.*, **107**, 8061, doi:10.1029/2001JD000623.
- Manabe, S., 1969: Climate and the ocean circulation: I. The atmospheric circulation and the hydrology of the earth's surface. *Mon. Wea. Rev.*, **97**, 739–774.
- , and R. J. Stouffer, 1996: Low-frequency variability of surface air temperature in a 1000-year integration of a coupled atmosphere–ocean–land model. *J. Climate*, **9**, 376–393.
- Marin, C. T., W. Bouten, and J. Sevink, 2000: Gross rainfall and its

- partitioning into throughfall, stemflow and evaporation of intercepted water in four forest ecosystems in western Amazonia. *J. Hydrol.*, **237**, 40–57.
- Matsuyama, H., 1992: The water budget in the Amazon river basin during the FGGE period. *J. Meteor. Soc. Japan*, **70**, 1071–1083.
- Matthews, E., 1983: Global vegetation and land use: New high-resolution data bases for climate studies. *J. Climate Appl. Meteor.*, **22**, 474–487.
- Nepstad, D. C., and Coauthors, 1994: The role of deep roots in the hydrological and carbon cycles of Amazonian forests and pastures. *Nature*, **372**, 666–669.
- , and Coauthors, 2002: The effects of partial throughfall exclusion on canopy processes, aboveground production, and biogeochemistry of an Amazon forest. *J. Geophys. Res.*, **107**, 8085, doi:10.1029/2001JD000360.
- Ogawa, K., and T. Schmugge, 2004: Mapping surface broadband emissivity of the Sahara Desert using ASTER and MODIS data. *Earth Interactions*, **8**. [Available online at <http://EarthInteractions.org>.]
- Oku, Y., and H. Ishikawa, 2004: Estimates of land surface temperature over the Tibetan Plateau using GMS data. *J. Appl. Meteor.*, **43**, 548–561.
- Oleson, K. W., G. B. Bonan, C. Schaaf, F. Gao, and Y. Jin, 2003: Assessment of global climate model land surface albedo using MODIS data. *Geophys. Res. Lett.*, **30**, 1443, doi:10.1029/2002GL016749.
- , and Coauthors, 2004: Technical Description of the Community Land Model (CLM). NCAR Tech. Note NCAR/TN-461+STR, 173 pp.
- Reale, O., and P. Dirmeyer, 2002: Modeling the effect of land surface evaporation variability on precipitation variability. Part I: General response. *J. Hydrometeor.*, **3**, 433–450.
- Rossow, W. B., and R. A. Schiffer, 1999: Advances in understanding clouds from ISCCP. *Bull. Amer. Meteor. Soc.*, **80**, 2261–2287.
- Sellers, P. J., and Coauthors, 1997: Modeling the exchanges of energy, water, and carbon between continents and the atmosphere. *Science*, **275**, 502–509.
- Shuttleworth, W. J., 1988: Evaporation from Amazonian rainforest. *Proc. Roy. Soc. London*, **B233**, 321–346.
- Tian, Y., R. E. Dickinson, L. Zhou, and M. Saikh, 2004a: Impact of new land boundary conditions from Moderate Resolution Imaging Spectroradiometer (MODIS) data on the climatology of land surface variables. *J. Geophys. Res.*, **109**, D20115, doi:10.1029/2003JD004499.
- , —, —, R. B. Myneni, M. Friedl, C. B. Schaaf, M. Carroll, and F. Gao, 2004b: Land boundary conditions from MODIS data and consequences for the albedo of a climate model. *Geophys. Res. Lett.*, **31**, L05504, doi:10.1029/2003GL019104.
- Ubarana, V. N., 1996: Observations and modelling of rainfall interception at two experimental sites in Amazonia. *Amazonian Deforestation and Climate*, J. H. C. Gash et al., Eds., Wiley, 151–162.
- Wang, Z., X. Zeng, M. Barlage, R. E. Dickinson, F. Gao, and C. B. Schaaf, 2004: Using MODIS BRDF and albedo data to evaluate global model land surface albedo. *J. Hydrometeor.*, **5**, 3–14.
- Wen, J., and Z. Su, 2003: Determination of land surface temperature and soil moisture from Tropical Rainfall Measuring Mission/Microwave Imager remote sensing data. *J. Geophys. Res.*, **108**, 4038, doi:10.1029/2002JD002176.
- Willmott, C. J., and K. Matsuura, cited 2000: Terrestrial air temperature and precipitation: Monthly and annual climatologies. [Available online at <http://climate.geog.udel.edu/~climate/>]
- Wilson, M. F., and A. Henderson-Sellers, 1985: A global archive of land cover and soils data for use in general circulation climate models. *J. Climatol.*, **5**, 119–143.
- Xie, P., and P. A. Arkin, 1997: Global precipitation: A 17-yr monthly analysis based on gauge observations, satellite estimates, and numerical model outputs. *Bull. Amer. Meteor. Soc.*, **78**, 2539–2558.
- Yang, Z.-L., Y. Dai, R. E. Dickinson, and W. J. Shuttleworth, 1999: Sensitivity of ground heat flux to vegetation cover fraction and leaf area index. *J. Geophys. Res.*, **104** (D16), 19 505–19 514.
- Zeng, X., M. Shaikh, Y. Dai, R. E. Dickinson, and R. Myneni, 2002: Coupling of the Common Land Model to the NCAR Community Climate Model. *J. Climate*, **15**, 1832–1854.
- , R. E. Dickinson, M. Barlage, Y. Dai, G. Wang, and K. Oleson, 2005: Treatment of undercanopy turbulence in land models. *J. Climate*, **18**, 5086–5094.
- Zhang, Y., W. B. Rossow, A. A. Lacis, V. Oinas, and M. I. Mishchenko, 2004: Calculation of radiative fluxes from the surface to top of atmosphere based on ISCCP and other global data sets: Refinements of the radiative transfer model and the input data. *J. Geophys. Res.*, **109**, D19105, doi:10.1029/2003JD004457.
- Zhou, L., R. E. Dickinson, Y. Tian, M. Jin, K. Ogawa, H. Yu, and T. Schmugge, 2003: A sensitivity study of climate and energy balance simulations with use of satellite-derived emissivity data over Northern Africa and the Arabian Peninsula. *J. Geophys. Res.*, **108**, 4795, doi:10.1029/2003JD004083.